# On the Annual Cycle, Variability, and Correlations of Oceanic Low-Topped Clouds with Large-Scale Circulation Using *Aqua* MODIS and ERA-Interim

TERENCE L. KUBAR, DUANE E. WALISER, J.-L. LI, AND XIANAN JIANG

*Jet Propulsion Laboratory, California Institute of Technology, Pasadena, California*

(Manuscript received 26 August 2011, in final form 15 February 2012)

ABSTRACT

Eight years of *Aqua* Moderate Resolution Imaging Spectroradiometer (MODIS) level-3 cloud data in conjunction with collocated Interim ECMWF Re-Analysis are used to investigate relationships between isolated low-topped cloud fraction (LCF) and dynamics/thermodynamics versus averaging time scale. Correlation coefficients between LCF and −SST exceed 0.70 over 56% of ocean regions from 25°S to 25°N for 90-day running means and exceed 0.70 between LCF and 500-hPa omega ($\omega_{500}$) for over one-third of oceans from 50°S to 50°N. Correlations increase most dramatically by increasing the averaging time scale from 1 day to about 15, owing to the large LCF synoptic variability and random effects that are suppressed by averaging. In five regions selected with monthly mean SSTs between 291 and 303 K, SST decreases by $-0.13\,\mathrm{K}\,\%^{-1}$ low-cloud cover increase. Monthly LCF is also correlated with estimated inversion strength (EIS), which is SST dominated in low latitudes and free tropospheric temperature dominated in the northeast Atlantic, Pacific, and midlatitudes, though SST and stability are poor predictors of LCF over the southern oceans.

Where the fraction of variance explained by the annual LCF harmonic is high, maximum LCF tends to lead minimum SST by ~15–30 days such that clouds can amplify the SST annual cycle, especially when LCF maxima coexist with insolation minima. Monthly mean LCF tends to scale with $\omega_{500}$ exponentially over the convective margins and offshore of the Pacific Northwest, but daily climatology relationships indicate that LCF levels off and even diminishes for $\omega_{500} > 0.05$ Pa $s^{-1}$, suggesting a limit through, perhaps, a too strong suppression of boundary layer heights. This suggests the need for dynamic-regime analysis in diagnosing low cloud/circulation feedbacks.

## 1. Introduction

Understanding the extent to which low-topped clouds are physically connected to the large-scale circulation of the atmosphere is of utmost importance in both constraining and improving estimates of the earth's climate sensitivity. Low-topped clouds profoundly modulate the radiation balance especially over the oceans due to the high albedo relative to the dark ocean surface. No consensus yet exists even on the sign of cloud feedbacks (negative or positive) in GCMs; models that show an increase in low-topped clouds with imposed greenhouse gas warming suggest a negative low-cloud feedback and have weak $2 \times CO_2$ climate sensitivities, and vice versa. This behavior in models is related to large-scale circulation changes; models that show a weakening, particularly of the Walker and Hadley circulations, tend to show fewer low-topped clouds with greenhouse gas forcing. A comprehensive review on the history and challenge of cloud–climate feedbacks can be found in Stephens (2005).

In addition to feedbacks associated with possible low-cloud changes with climate warming, low-topped clouds are also significant in modulating the SST annual cycle, particularly in the eastern equatorial region and certain subtropical areas. In an oceanic observational analysis of the heat content annual cycle off the Peruvian coast by Takahashi (2005), pervasive low-level stratus and stratocumulus clouds present over dynamically forced upwelling cold SST regimes amplify the SST annual cycle amplitude, primarily by reducing insolation with near-maximum shading (shortwave effect) when insolation is near a minimum. Cold low-level atmospheric temperature advection, which in the Peruvian region leads low clouds by one to two months (Takahashi 2005),

*Corresponding author address:* Terence L. Kubar, Jet Propulsion Laboratory, California Institute of Technology, MS 233-300, 4800 Oak Grove Drive, Pasadena, CA 91109.
E-mail: terry.kubar@jpl.nasa.gov

DOI: 10.1175/JCLI-D-11-00478.1

is important for low-cloud formation because of the induced upward sensible and latent heat fluxes (Klein 1997).

A number of studies have also shed light on the significance of low-topped clouds in terms of maintaining tropical SSTs, tropical circulation, and variability. Subsiding dry air above a cold surface is statically stable and favorable for abundant low-level stratus clouds (Mitchell and Wallace 1992; Klein and Hartmann 1993). As demonstrated in Rodwell and Hoskins (2001), the presence of the Andes Mountains in western South America maintains cold equatorward flow parallel to the coast. Idealized coupled ocean–atmosphere GCMs have highlighted the importance of reflective low-level clouds to the strength of the Hadley and Walker circulations, SST annual cycle, and asymmetries in the eastern near-equatorial Northern versus Southern Hemisphere, with the ITCZ being constrained to the Northern Hemisphere (Philander et al. 1996; Ma et al. 1996; Yu and Mechoso 1999; Takahashi and Battisti 2007).

Investigations from satellite and surface-based cloud observations of cloud sensitivity and feedbacks with SST have been quite numerous in various regions and time scales. Over the southeastern Pacific and Atlantic stratocumulus regions, Oreopoulos and Davies (1993) use Earth Radiation Budget Experiment (ERBE) and International Satellite Cloud Climatology Project (ISCCP) data for cloud fraction and optical depth, respectively, to show decreases in both with increasing SST. In another study, Norris and Leovy (1994) examine a large area (tropics and midlatitudes) and long surface dataset (Global Distribution of Total Cloud Cover and Cloud Type Amounts over the Ocean; see Hahn et al. 1998; Warren et al. 1988) of 30 yr to quantify negative and statistically significant correlations between marine stratiform cloudiness (MSC) and SST anomalies at the seasonal time scale, particularly during the Northern Hemisphere summer in the North Pacific midlatitudes, eastern subtropical oceans, and eastern tropical Pacific. The largest negative correlations are found over the strongest SST gradients, rather than at locations of maximum MSC. Also, midlatitude summertime MSC is collocated with warm surface advection, with no lag between SST and MSC anomalies, whereas in the subtropics cold surface advection dominates and SSTs lag MSC seasonal maxima by up to several months.

A number of studies have also investigated composite cloud relationships as a function of dynamic regime. Especially in areas of large-scale mean subsidence, Bony et al. (1997) show that cloud fraction, cloud optical thickness, and shortwave cloud forcing decrease with increasing SST, with cloud-top pressures greater than ~650 hPa primarily for SSTs $\lesssim$298 K, after which SST free tropospheric ascent becomes much more likely until SSTs exceed 302.5 K when subsidence becomes more likely. Ascent and deep convection over a narrow range of SSTs is consistent with satellite and European Centre for Medium-Range Weather Forecasts-Year of Tropical Convection (YOTC) vertical velocity analyses in a northeast Pacific cross section from California to the central equator in Kubar et al. (2011).

A recent study (Eitzen et al. 2011) has also examined low-cloud feedbacks in primary low-cloud regions around the globe using monthly gridded data from Clouds and the Earth's Radiant Energy System (CERES) *Terra* Moderate Resolution Imaging Spectroradiometer (MODIS) data as a function of SST anomalies. This is consistent with Bony et al. (1997), with decreasing cloud fraction and optical depth with increasing SST anomalies, albeit with an increasingly less negative total cloud radiative effect with those anomalies. An inverse relation between estimated inversion strength (EIS) and SST is seen as responsible for observed decreases of cloud fraction and optical depth with SST. Estimated inversion strength encompasses the observation that the free-tropospheric temperature often closely adheres to the moist adiabatic lapse rate (Wood and Bretherton 2006), which is stronger for a given lower tropospheric stability (LTS) $\theta_{700} - \theta_{\mathrm{sfc}}$, Klein and Hartmann 1993) for colder temperatures. Thus, LTS variations are more temperature dependent rather than inversion strength dependent compared to EIS. On monthly and longer time scales, EIS explains 83% of low-cloud cover variance in selected tropical, subtropical, and midlatitude regions.

In many of the aforementioned studies, monthly or seasonal rather than synoptic-scale variations are examined, but shorter-term variability at one location in the North Pacific is the subject of Klein (1997). While no single variable can explain more than 13% of low-cloud variance on daily time scales, correlations improve with temporal averaging of multiple days, and averaging ~10 days yields correlations almost as high as monthly means. Synoptic variables most related to low clouds are cold advection, low-level stability, and cloud-level RH. Free-tropospheric vertical velocity, which also controls inversion strength and height, is not explicitly examined in Klein.

Subseasonal low cloud variability has also been examined over the southeastern Pacific. Xu et al. (2005) show that enhanced surface southeasterly winds and cold advection there, associated with higher sea level pressure (SLP) anomalies (stronger anticyclone), lead cloud liquid water by 1–2 days, suggesting the importance of the atmospheric circulation on short time scales. George and Wood (2010) find that low-cloud albedo variations are primarily driven by cloud fractional variations (except less so very close to South America) and

that variability of meteorological variables such as SLP, temperature advection, and stability explains most cloud property variance, though correlations are not especially strong with any one variable on short time scales, as in Klein (1997).

We expand upon previous subseasonal analyses, which have tended to be more regional or larger-domain studies, that have focused more on seasonal or interannual scales to examine relationships of large-scale dynamics and low-cloud properties over the oceans between 50°S and 50°N, ranging from daily variations to the annual cycle in grids free of middle and high clouds. We include the entire annual cycle to calculate correlations and do not examine anomalies. We also quantify the extent to which the annual harmonic explains the variance of clouds and SSTs and construct maps of lead/lag analysis so as to identify regions of possible internal feedbacks such as between clouds and SSTs, particularly where clouds maximize during minimum insolation. We also examine daily climatological variability of clouds and $\omega_{500}$ since both exhibit significant synoptic-scale variance.

We furthermore expand upon previous work examining stability and low cloud relationships by constructing correlation maps to see where stability (e.g., EIS, LTS) is SST versus free tropospheric dominated. Our analysis is established to serve as a test bed for climate models in resolving proper short temporal scale and annual cycle relationships with implications for future changes under global warming.

## 2. Observational and analysis/reanalysis datasets

### a. MODIS level 3

Our primary observational dataset is the Moderate Resolution Imaging Spectroradiometer(MODIS) level-3 (L3) daily product (Hubanks et al. 2008) (collection 051) for which we use eight full years between October 2002 and September 2010. The MODIS L3 product is already gridded at 1° × 1° based on native resolution pixel data at 1, 5, or 10 km depending on the variable, and we use version 051. MODIS is a 36-band instrument aboard both the *Aqua* and *Terra* satellites, though we restrict our analysis here to *Aqua*, which contains equatorial crossing times 0130 and 1330 local time. *Aqua* was chosen partly because it is part of the A-Train constellation and, as such, relationships can be more readily compared to other A-Train instruments, for example, Cloud–Aerosol Lidar and Infrared Pathfinder Satellite Observations (CALIPSO), *CloudSat*, in the future. We only use daytime MODIS data so that all MODIS statistics at each location are based on the same time at that location. Usage of daytime-only data does not permit observations of the diurnal cycle, although the boundary layer/low cloud diurnal cycle has been rather thoroughly investigated (e.g., Minnis and Harrison 1984; Rozendaal et al. 1995; Zuidema and Hartmann 1995; Weng and Grody 1994; Greenwald and Christopher 1999; Wood et al. 2002; and to some extent Behrangi et al. 2012), and we do not attempt to include this as well in our study, as the focus is more on the annual cycle. Eight full years of once-daily data at each location is more than sufficient to allow extensive analysis of statistical relationships between low clouds and the large-scale circulation. A more complete background on pertinent MODIS L2 products used for L3 variables in our study, including cloud mask, flags, and cloud top and optical properties, can be found in Platnick et al. (2003), and extensive sampling information and statistical information within each L3 1° × 1° box is described in Hubanks et al. (2008).

### b. ERA-Interim

Sea surface temperatures, sea level pressure, surface temperature advection, and pressure vertical velocity at 500 mb ($\omega_{500}$) all come from the Interim ECMWF Re-Analysis (ERA-Interim) (Simmons et al. 2006), available four times daily but for which we average for daily means. Data for this product that we use include surface data and pressure-level data for which 37 pressure levels exist; the horizontal resolution is 1.5° × 1.5°. The ERA-Interim is considered to be the best reanalysis product available, and the number of observations assimilated into this version has increased by an order of magnitude since the previous version [40-yr ECMWF Re-Analysis (ERA-40)]. Included in assimilated observations are geostationary satellite motion vectors, scatterometer near-surface wind data, and other observations for surface pressure, wind, and temperature. As shown extensively in Dee et al. (2011), significant improvements have occurred in ERA-Interim versus ERA-40.

## 3. Definitions and methods

### a. Determination of 1° × 1° low-cloud grids

As the primary focus of our study is low clouds and their relationships globally to large-scale environmental variables, we restrict our definition of low-cloud grids to those, in which we are confident to the best of our ability, that contain no upper-level cloudiness. This sets our study apart from others that have attempted to estimate total low-cloud fraction, even in the presence of overlapping or adjacent higher-topped clouds, and thus may be associated with different large-scale dynamic regimes

versus areas of isolated low-topped clouds. Using the MODIS cloud mask L3 product, to be classified as a pure 1° low-cloud grid, *all* pixels must adhere to one of two sets of conditions: 1) either all clouds must have cloud tops warmer than 270 K and top pressures greater than 500 hPa, as detected by MODIS, which are the same temperature and pressure definitions used in Kubar et al. (2011), or 2) mean cloud top temperature may be below 270 K, but all pixels must have cloud top pressures greater than 500 hPa and the minimum temperature must be less than 10 K colder than the 1° × 1° box mean; furthermore, estimated mean cloud top height must be less than 4 km. The restriction $\Delta T_{\mathrm{TOP}}$ of 10 K is included to reduce the likelihood of high-topped clouds, and estimated cloud heights are computed following Zuidema et al. (2009) in which the mean boundary-layer lapse rate is assumed, SST is used from the ERA-Interim, and cloud top temperature is used from MODIS, as follows:

$$z_{\mathrm{top}}(m) = \frac{\mathrm{SST} - T_{\mathrm{TOP(MODIS)}} - 2.35}{0.0069}. \qquad (1)$$

The constant 2.35 in (1) is an addition of 1.05 K from the best-fit line and a 1.3-K offset in which MODIS cloud top temperatures are statistically this much lower than the radiosonde-derived inversion bases. As reported in Zuidema et al., the correlation coefficient between MODIS cloud top temperatures and inversion base heights from radiosondes is 0.73. We use (1) to ensure that no clouds with tops below 270 K are excessively deep (4 km) rather than precisely assessing cloud top heights. We include the second set of conditions above so that midlatitude clouds, which may be quite low in height albeit colder than 270 K, are included in our tropical and midlatitude low-topped cloud analysis.

Grids abiding by one of the two above low-cloud definitions are called PURE_LOW, and low cloud fractions within PURE_LOW are called LCF. For a 1° × 1° grid to be considered for classification using statistical analysis (PURE_LOW or other), we require that the grid contains a minimum of 50 valid (nonmissing) pixels, which is thus a minimum of greater than 10% of possible observations (maximum 484) across the box. If the mean cloud fraction of the 1° × 1° grid is one, we then use that as the cloud fraction but, if it is less than one, we compute cloud fraction by considering the pixel number within each cloud fraction histogram bin (based on the distribution of 5-km pixels) as provided by MODIS as 0.1, 0.3, 0.5, 0.7, and 0.9. We save all pixel counts and histogram information rather than simply mean cloud fraction values as given by MODIS so that 1° × 1° grids with more valid observations are weighted accordingly. This method retains more of the higher native resolution pixel information important for statistical analysis.

Invoking the maximum overlap assumption as has been done in some previous studies and is a common approach to estimate the total amount of low clouds, some of which may be masked by the presence of higher-topped clouds, is not considered in our study as we are most interested in the dynamic and SST regimes associated directly with 1° × 1° scenes absent of higher-topped clouds. The dynamical state may control other cloud types as well, but presumably it also is physically connected whether or not PURE_LOW exists, as well as the properties within. In this way, capturing grids with only lower-topped clouds is somewhat closer to the boundary-layer cloud object method, as defined and analyzed in Xu et al. (2005) and Eitzen et al. (2008), in which the physical properties of contiguous satellite cloud footprints are assessed. Scenes are excluded in those studies that contain clouds deeper than a certain height (e.g., 3 km) to purely look at boundary cloud objects, much as we examine PURE_LOW for 1° × 1° boxes. Finally, our metric of excluding grids with upper-level cloudiness defines low-cloud-only grids that may readily be compared with climate models.

### b. Large-scale variables

As discussed and demonstrated by Klein (1997), Ronca and Battisti (1997), Wylie et al. (1989), and Bretherton et al. (1995), low-level cold advection, particularly in eastern boundary subtropical regimes, can be physically connected to low clouds because of the induced upward sensible and latent heat fluxes that heat the boundary layer from below, important for low-cloud formation. For our 8-yr analysis of thermodynamics and dynamics we use ERA-Interim, and surface temperature advection in the horizontal is defined as

$$\mathrm{SFC\_TEMP\_ADV} \equiv -u\frac{\partial \mathrm{SST}}{\partial x} - v\frac{\partial \mathrm{SST}}{\partial y}, \qquad (2)$$

where $u$ and $v$ are the 10-m east/west and north/south winds, respectively. Temperature advection is calculated by centered finite differencing.

While surface cold advection tends to be commonly associated with low clouds in the tropics and subtropics, particularly in favorable regions around subtropical high pressure circulations (e.g., the eastern boundaries) or during cold-air outbreaks during winter off the east coasts of Asia and North America (Li 1994), Norris (1998a,b) and Norris and Klein (2000) demonstrate that particular low cloud types, especially fair-weather and bad-weather stratus, are also associated with warm

surface advection and synoptic ascent, especially in favored midlatitudes regions. While we do not specifically examine different low cloud types in this study, PURE_LOW potentially encompasses several low cloud types, but only those not directly connected or obscured by high-topped clouds.

We also devote a good portion of space in this manuscript to examining the statistical relationships of different variables as a function of averaging time. In terms of understanding connections of low clouds to environmental variables such as SST, SFC_TEMP_ADV, and $\omega_{500}$, etc., we retain pixel-level cloud information from each of the valid 1° boxes and aggregate these into 4° × 4° boxes for each day to determine the mean cloud fraction and environmental variable in question, and then perform correlation analysis to find the linear Pearson correlation coefficient either on the daily time scale or by examining the running mean (e.g., 5 days, 15 days). We aggregate pixel information onto 4° × 4° boxes when examining correlations, the annual cycle, and relationships with the ECMWF dynamical variables, primarily to ensure adequate sampling at the daily time scale. Finally, we require each 1° × 1° box to contain a minimum of 50 valid pixels to be used in the analysis.

For completeness and to build upon previous studies, we also perform correlation analysis of LCF at the monthly time scale with two stability parameters (LTS and EIS) and 700-hPa temperature, and thus assess the extent to which cross-correlation exists among these stability measures and large-scale dynamics. This allows an assessment between 50°S and 50°N of low-level versus free-troposphere controlled stability regions.

As mentioned, we are also interested in quantifying the annual cycle of low clouds over the oceans between 50°S and 50°N and environmental variables fundamentally related to low clouds, to not only better understand the coherence (temporally), but also the extent to which variability can be explained by this harmonic. To do this, we calculate the detrended daily ''climatology'' of all variables within each 4° × 4° box for the entire 8-yr period between October 2002 and September 2010, and use the Interactive Data Language (IDL) fast Fourier transform (FFT) function to solve the following:

$$Y_x = \frac{2}{365}\sum_{t=0}^{364} \exp(2\pi it/365)x(t + t_0), \qquad (3)$$

where $x(t + t_0)$ is the demeaned time series (e.g., LCF, SST), which encompasses positive and negative frequencies, as in Stine et al. (2009). The phase (e.g., minimum SST, maximum LCF) is determined by using the inverse FFT of $x(t + t_0)$ to compute $\theta_x = \tan^{-1}[\mathrm{Im}\,(Y_x)/\mathrm{Re}\,(Y_x)]$ and the amplitude by taking the absolute value of the forward FFT of $x(t + t_0)$. The fraction of variance explained by the annual cycle is found by taking the variance of the annual cycle and dividing by the total variance of all frequencies, and the climatology of the 4° × 4° box is valid only if at least 362 days contain valid data.

## 4. Mean state and correlation analysis

### a. Mean seasonal vertical velocity and LCF

To acquire insight into the large-scale mean circulation and associated low-cloud cover over the entire 8-yr period, we start by looking at the annual mean $\omega_{500}$ and LCF, shown in Figs. 1a,b and plotted at 1.5° × 1.5° and 1° × 1°, respectively. On the global scale extensive areas of low-topped clouds are found where the atmosphere is subsiding, as this limits vertical growth of clouds primarily to the boundary layer. Negative values of $\omega_{500}$ indicate midtropospheric rising motion and positive values sinking motion. The intertropical convergence zone is well-indicated by rising motion in the tropics extending across the globe, and the South Pacific convergence zone (SPCZ) by a wide band of ascent over the Southern Hemisphere. Large-scale subsidence regions are found in five major clusters around the world, primarily in the subtropics, and also along the eastern Pacific equatorial cold tongue. Areas of maximum LCF are broadly aligned with regions of mean subsidence, particularly over the eastern ocean boundaries where annual mean SSTs are lower than in other regions along the same longitude, as shown in Fig. 1c. We also show the subsidence frequency of occurrence (frequency in which $\omega_{500} > 0$ Pa $s^{-1}$) (Fig. 1d), generally portraying the same story as mean $\omega_{500}$.

Relatively large season-to-season differences exist not only in the strength and location of mean subsidence, but also in both amount and location of low-topped cloud cover; we show seasonal $\omega_{500}$ and LCF in Fig. 2. For brevity, we only show June–August (JJA) and December–February (DJF). Here we see that seasonal LCF shifts in location and amount in general correspondence with the location of the occurrence of midtropospheric subsidence. For instance, during DJF a wide swath of greater LCF in the 20°N latitude band across the Pacific and Atlantic is aligned with that same subsidence band. During JJA, in contrast, subsidence in the Northern Hemisphere extends well poleward across the eastern Atlantic and Pacific basins, and the corresponding LCFs in those regions are maxima. The location and extent of subsidence in the Southern Hemisphere tend to vary less with season, though the general qualitative

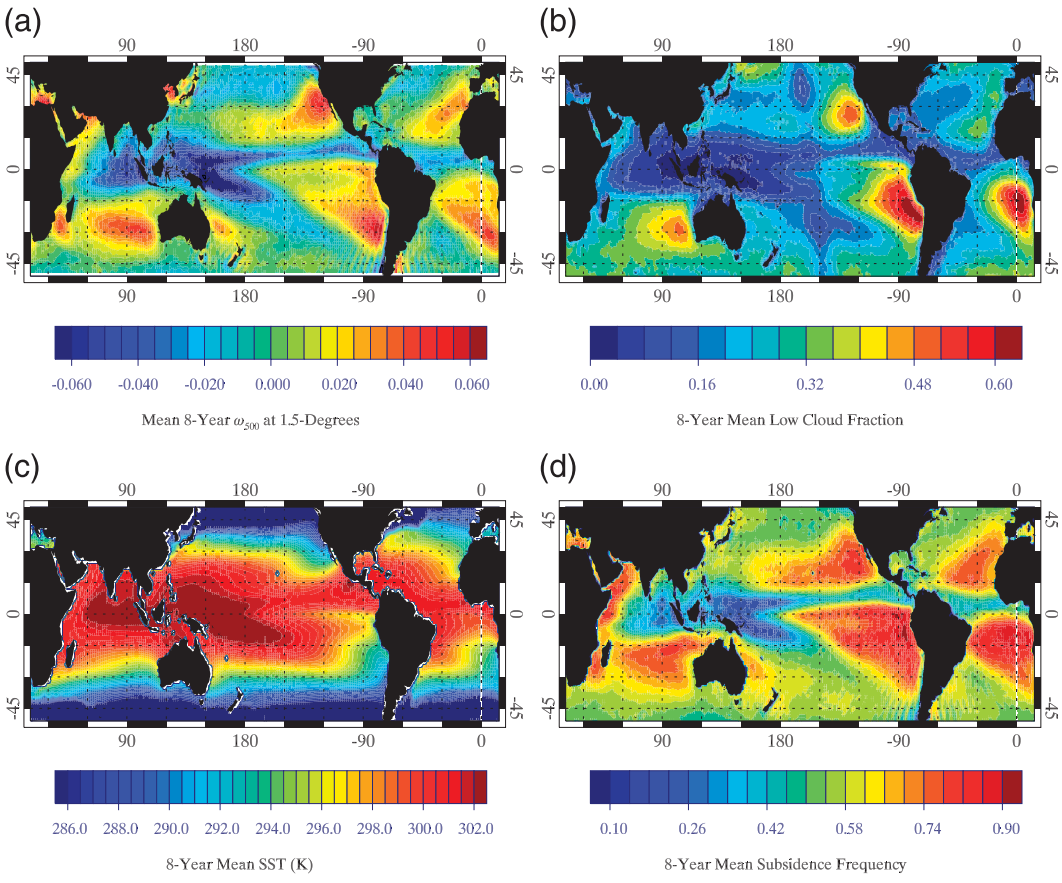


FIG. 1. (a) An 8-yr mean $\omega_{500}$ (Pa s$^{-1}$), (b) LCF, (c) SST (K), and (d) subsidence frequency. Cloud data are from MODIS *Aqua*, and SSTs and $\omega_{500}$ from ERA-Interim.

correspondence between broad regions of subsidence and LCF is still apparent.

At this point, it is worth underscoring that our LCF values are lower, particularly in some midlatitude regions, compared to surface-based low-topped cloud observations, as our LCF comes from $1° \times 1°$ grids that only contain clouds either warmer than 270 K or with tops below 4 km and pressure tops greater than 500 hPa. In the northern summer midlatitudes north of 40° over the central Pacific LCF maximizes at $0.30 \sim 0.35$ (except higher in the far northeast Pacific), though significant amounts of midlevel clouds and even some high clouds exist especially in the north-central Pacific, whose presence would not meet our PURE_LOW criteria. Indeed, Rozendaal et al. (1995) indicate that, even with a random overlap assumption invoked to correct for the presence of middle and high clouds, the northwest Pacific and Southern Hemisphere (south of ~30°S) corrected low cloud cover from ISCCP is still somewhat lower than surface-based values from the *Cloud Atlas*. This is a possible shortcoming of that assumption, and the positive correlation between low clouds and higher clouds in that region is a problem that our analysis avoids, as our screening process only assesses PURE_LOW grids. These PURE_LOW grids are also more fundamentally related to the cloud forcing associated with low cloud scenes only. Finally, it is important to note that mean ascent is observed during JJA in the north-central and northwestern Pacific such that low clouds in isolation are less likely.

Though regions of large-scale subsidence coincide with greater LCF in the mean sense, even by season, we can also conditionally evaluate how sensitive LCF is to whether the midtroposphere is rising or sinking. Even mean-state subsidence regions are occasionally disrupted either by synoptic frontal systems primarily in midlatitudes or parts of the subtropics (during local winter) or even occasional convective activity during certain periods or seasons. In Fig. 3, we show the difference in LCF between days of large-scale subsidence ($\omega_{500} > 0$ Pa s$^{-1}$) and ascent ($\omega_{500} < 0$ Pa s$^{-1}$), or sinking LCF and rising LCF. We have chosen a common grid for the analysis of low clouds and subsidence/ascent of $4° \times 4°$ here. This shows that, except near the equator where

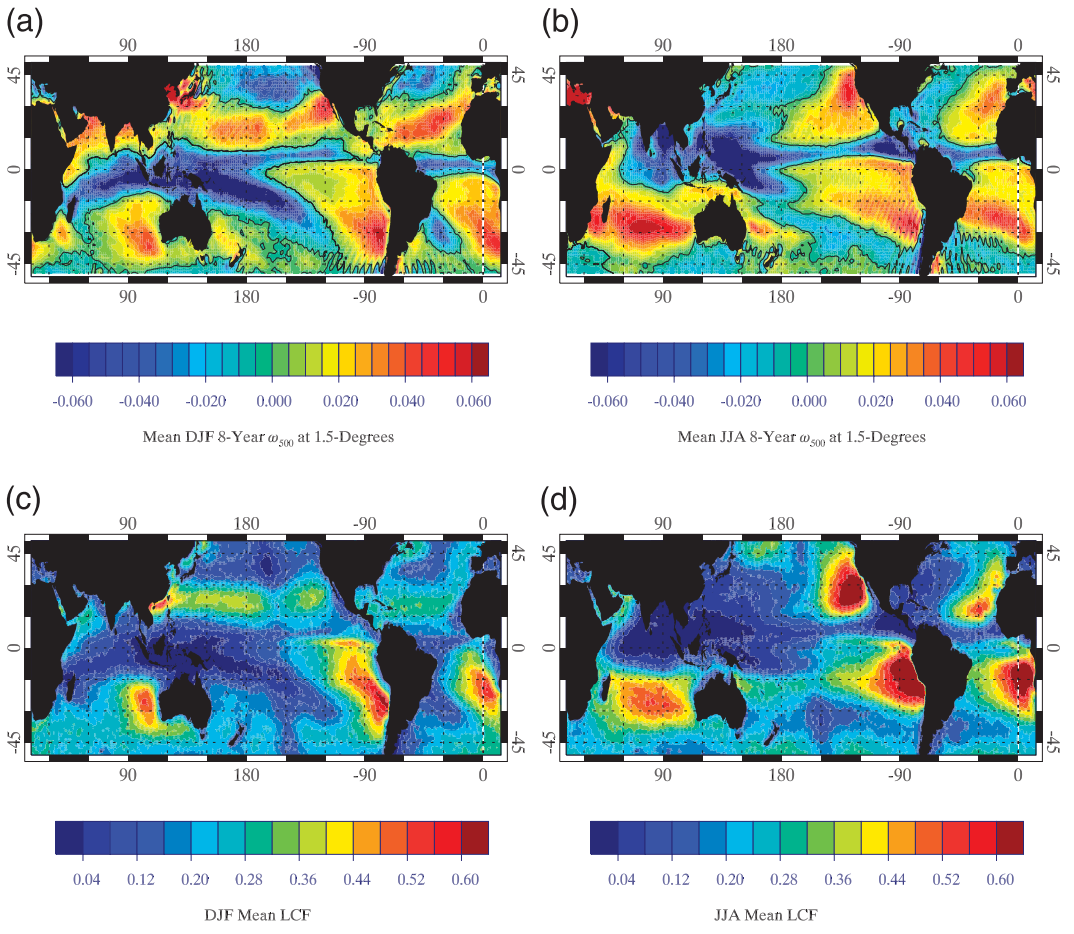


FIG. 2. (a) An 8-yr mean DJF $\omega_{500}$, (b) mean JJA $\omega_{500}$, (c) DJF mean LCF, and (d) JJA mean LCF.

very few low clouds exist in isolation due to deep convection, sinking LCF − rising LCF is positive nearly everywhere and much larger over the subtropics and midlatitudes, especially in the eastern Pacific, parts of the central Pacific, and the southern Indian Ocean. From 50°S to 50°N daily sinking LCF is 0.29 and rising LCF is 0.15.

We also examine sinking LCF − rising LCF on a 10-day time scale in Fig. 3b for which we evaluate the difference in LCF when the 10-day running mean of $\omega_{500}$ is positive versus negative. Some small areas cannot be assessed where 10-day $\omega_{500}$ sinking or rising conditions do not exist, and these areas are shown in white. Generally, the 10-day differences are fairly similar to the daily differences, albeit overall areal coverage where sinking LCF – rising LCF $> 0.1$ is smaller, especially in the midlatitudes. Ten-day sinking LCF − rising LCF is slightly higher than in the daily analysis over the central equatorial Pacific, where inactive periods of deep convection associated with 10-day mean subsidence permit more isolated shallow clouds. Since a 10-day period encompasses synoptic variability, even a mean 10-day subsidence region may not ensure subsidence during each of the 10 days, therefore reducing sinking LCF − rising LCF in some areas.

In Figs. 3c,d, we show the LCF associated with daily sinking and rising conditions, respectively. These plots underscore that LCF globally is much higher when the midtroposphere is subsiding, though over the southeast Pacific and Atlantic, which nearly always exhibit free-tropospheric subsidence, the differences are quite small. Some ongoing work, particularly in the southeast Pacific, suggests instead that Rossby-wave-induced bands of subsidence on a multiday time scale may be aligned with low cloud systems, and this preliminary work emphasizes that simply asking whether or not the atmosphere is rising or sinking may not be sufficient to address whether LCF is considerably higher in some regions.

We next examine both SFC_TEMP_ADV and mean SLP during JJA and DJF (Fig. 4), which represents boreal winter and summer, respectively. During both

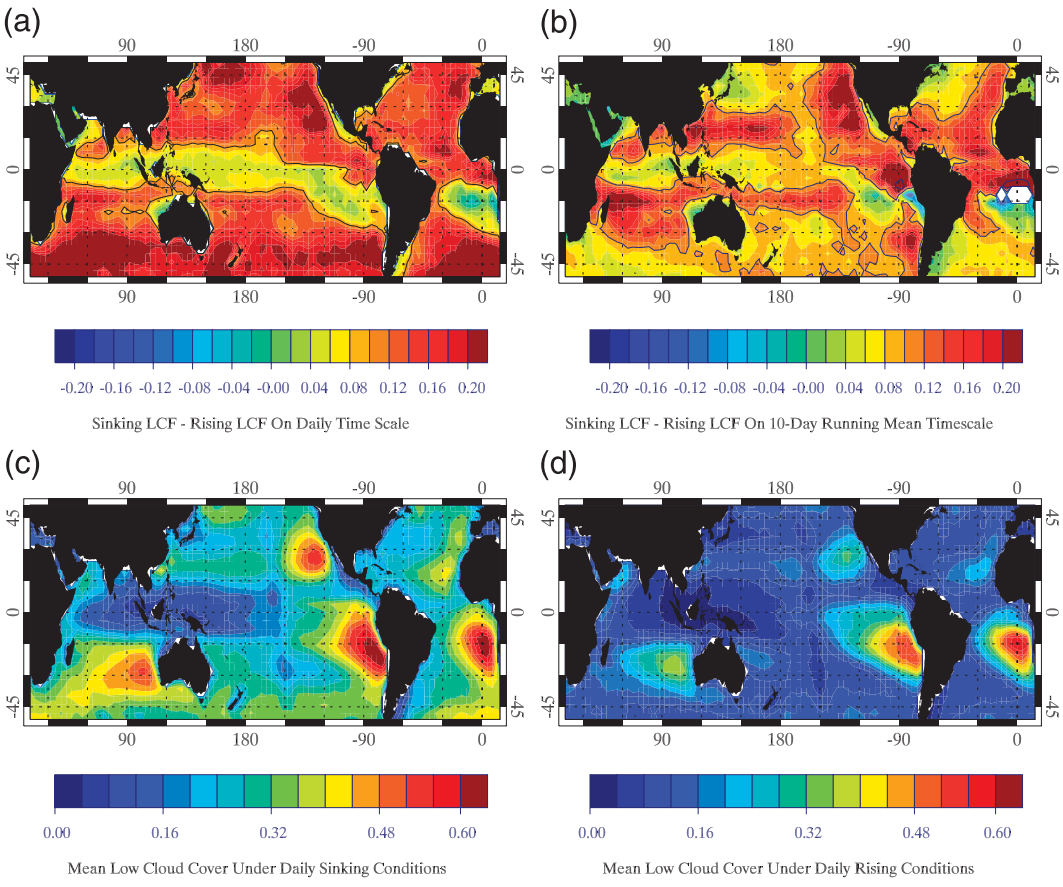


FIG. 3. (a) Daily sinking LCF minus rising LCF, in which sinking is for all days when $\omega_{500} > 0$ Pa s$^{-1}$ and rising when $\omega_{500} < 0$ Pa s$^{-1}$ and (b) for 10-day running mean sinking and rising. (c) LCF under daily subsidence and (d) LCF under daily ascent. Contours in (a) and (b) represent $\Delta CF > 0.1$.

DJF and JJA surface cold advection is most prevalent over the eastern subtropical ocean basins in both hemispheres as well as just to the north of the equator in both the eastern Pacific and Atlantic, though cold advection just north of the equator is stronger during JJA. Cold advection during JJA in the Northern Hemisphere is stronger, associated with circulation around the stronger subtropical highs, which are also centered poleward compared to DJF. Over the Southern Hemisphere the subtropical highs are semipermanent during summer (DJF) and winter (JJA), though during winter the high over the southern Indian Ocean is much stronger, also when the low cloud area in the southern Indian Ocean is more expansive (Fig. 2c).

During DJF the Aleutian low centered near the international date line around ~50°N becomes well-entrenched, and year-round warm SST advection in parts of the northern Pacific and Atlantic is apparent in association with the southerly component surface flow. As mentioned, both fair-weather and bad-weather stratus in this region are associated with warm surface advection and synoptic ascent, especially over the North Pacific (Norris 1998a,b; Norris and Klein 2000). Finally, during DJF the edge of a high centered over Asia is visible off the East China Sea and near Japan, and cold SST advection is prevalent over the far western Pacific, particularly during cold air outbreaks. We already saw that LCF is greater during DJF in this region, particularly around 20°N and even farther poleward just off the coast.

### *b. Correlation analysis as a function of time scale*

We now quantify LCF as a function of different variables of interest on various time scales, ranging from daily to long-term running means, to not only identify *where* large-scale variables are important but also *when* they become so. As in the previous section, our map analyses are conducted at 4° × 4° scales. We first test LCF against −SST and show global correlation maps (50°S–50°N) in Fig. 5 on daily, 5-day–, 15-day–, and 90-day running mean scales. In this analysis (and others hereafter), running means of LCF and −SST

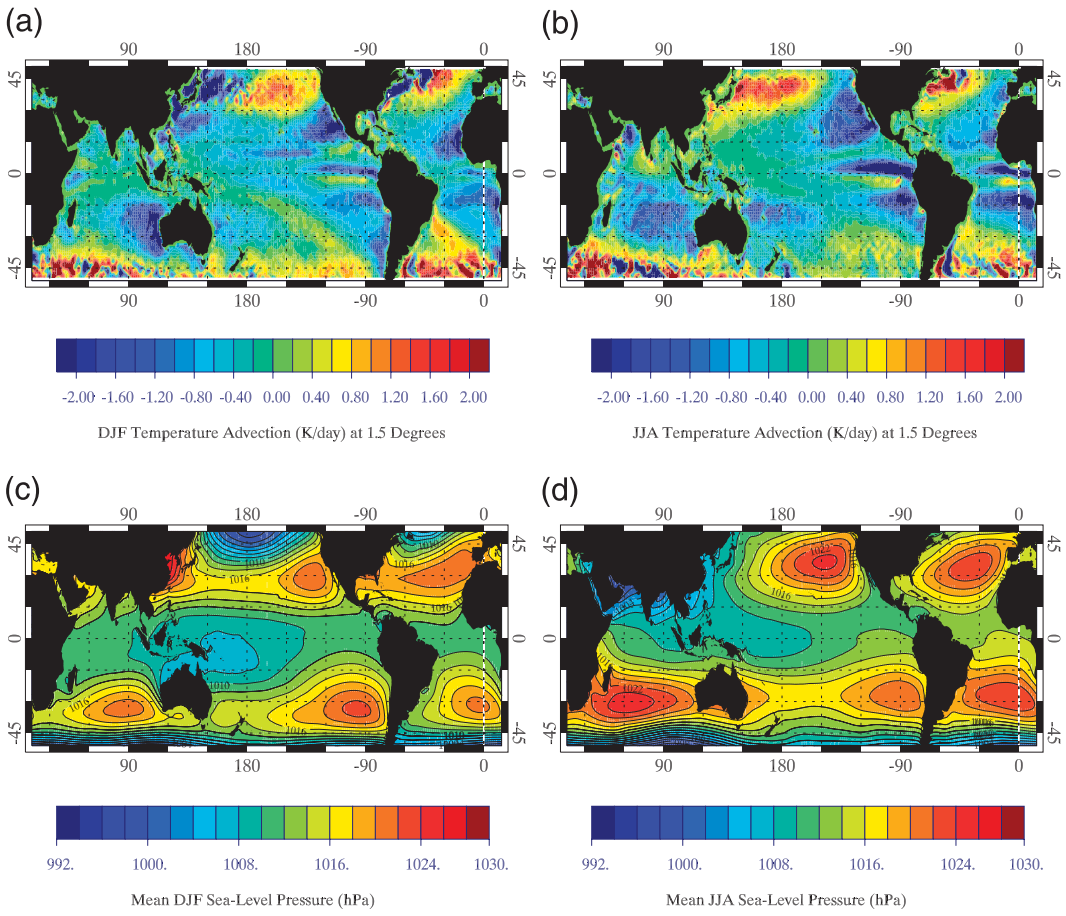


FIG. 4. (a) DJF SFC_TEMP_ADV (K day$^{-1}$), (b) JJA SFC_TEMP_ADV, (c) DJF SLP (hPa), and (d) JJA SLP.

are computed and then correlated within each box for the entire 8-yr period. In general, LCF is weakly correlated with −SST on the daily time scale, though modest positive LCF/negative SST correlations exist over the west Pacific near 20°N, over the eastern equatorial Pacific, and over much of the Southern Hemisphere to ~20°. Moderate positive LCF/−SST correlation regions become more pronounced by averaging five days together, and 15-day averages show that many regions have $r > 0.70$ (denoted by black contoured lines), as this value represents ~50% of LCF variance explained by SST. By averaging over 90 days, the strong positive LCF/−SST $r$ values encompass much of the lower latitudes between 25°S and 25°N, save for the near-equatorial western Pacific and Indian warm pools and all of the northeast Pacific down to ~20°N. Correlation coefficients exceed 0.70 over 56% of the region between these latitudes at the 90-day averaging scale. In contrast, LCF and −SST are *negatively* correlated in much of the Northern Hemisphere eastern Pacific, North Pacific, and eastern Atlantic. The switch from strong positive correlations to modest negative LCF/−SST correlations in the Pacific occurs south of ~30°N in the west Pacific and just south of ~20°N in the east Pacific. Over the northeastern Pacific, low clouds peak during summertime, when SSTs are higher than during winter but when subsidence and the North Pacific subtropical high are stronger and extend farther north. We will briefly see later that LCF in this northeastern subtropical Pacific is linked to stability, which is driven there by free tropospheric temperature much more strongly than SSTs.

In Figs. 5e,f, we present the sensitivity of LCF to a decrease in SST, or ΔLCF/(−ΔSST), which thus represents the slope of the best-fit line calculated in the above correlation analyses. We show maps at 30-day and 60-day averaging time scales when correlations are stronger. The slopes are especially high in pockets between 20°S and 20°N, where correlations exceed 0.70 [ΔLCF/(−ΔSST) ~ 0.07 K$^{-1}$], which is qualitatively similar but higher than in other studies that have looked at low cloud dependence on SSTs (e.g., Oreopoulos and Davies 1993; Bony et al. 1997; Eitzen et al. 2011; this is discussed in greater detail in the summary section).

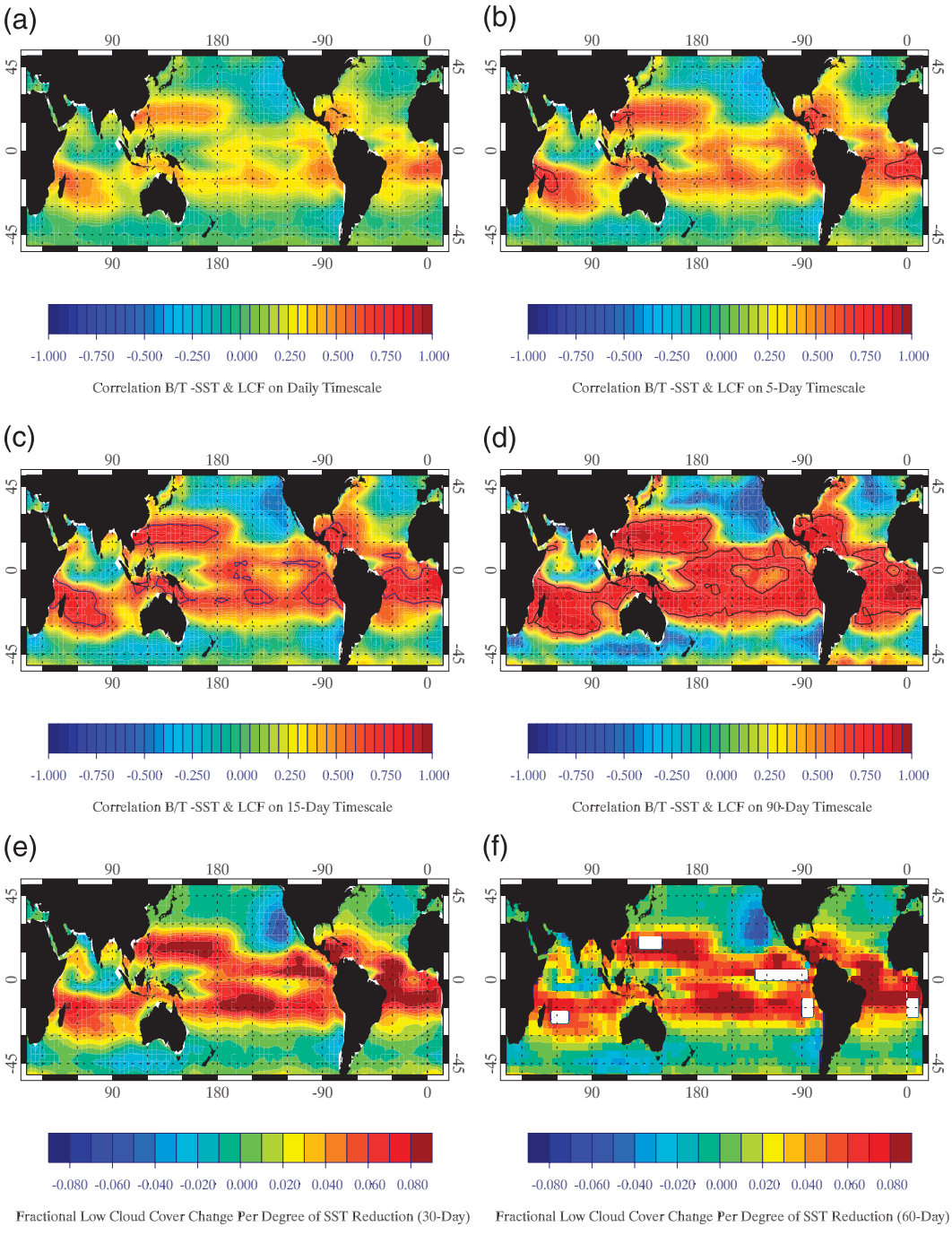


FIG. 5. Correlations between negative SST and LCF on (a) daily scale, (b) 5-day running mean, (c) 15-day running mean, and (d) 90-day running mean. ΔLCF per degree of SST reduction on (e) 30-day and (f) 90-day time scale. Black contours represent $r > 0.7$. White areas in (f) are regions specifically analyzed in Fig. 6.

To look more closely at locations where LCF is tightly correlated with decreasing SST, we examine monthly mean SST against LCF in five regions in the tropics and subtropics, giving each region 96 observations of clouds and SSTs. Here we plot SST versus LCF since LCF maxima tend to lead SST minima, with the suggestion that clouds in these regions may be modulating SSTs (discussed further in the annual cycle analysis in section 5). We choose the Peruvian (10°–20°S, 80°–90°W) and Namibian (10°–20°S, 0°–10°E) stratocumulus regions defined by Klein and Hartmann (1993), eastern equatorial Pacific (0°–5°N, 130°–175°W), west Pacific ~20°N

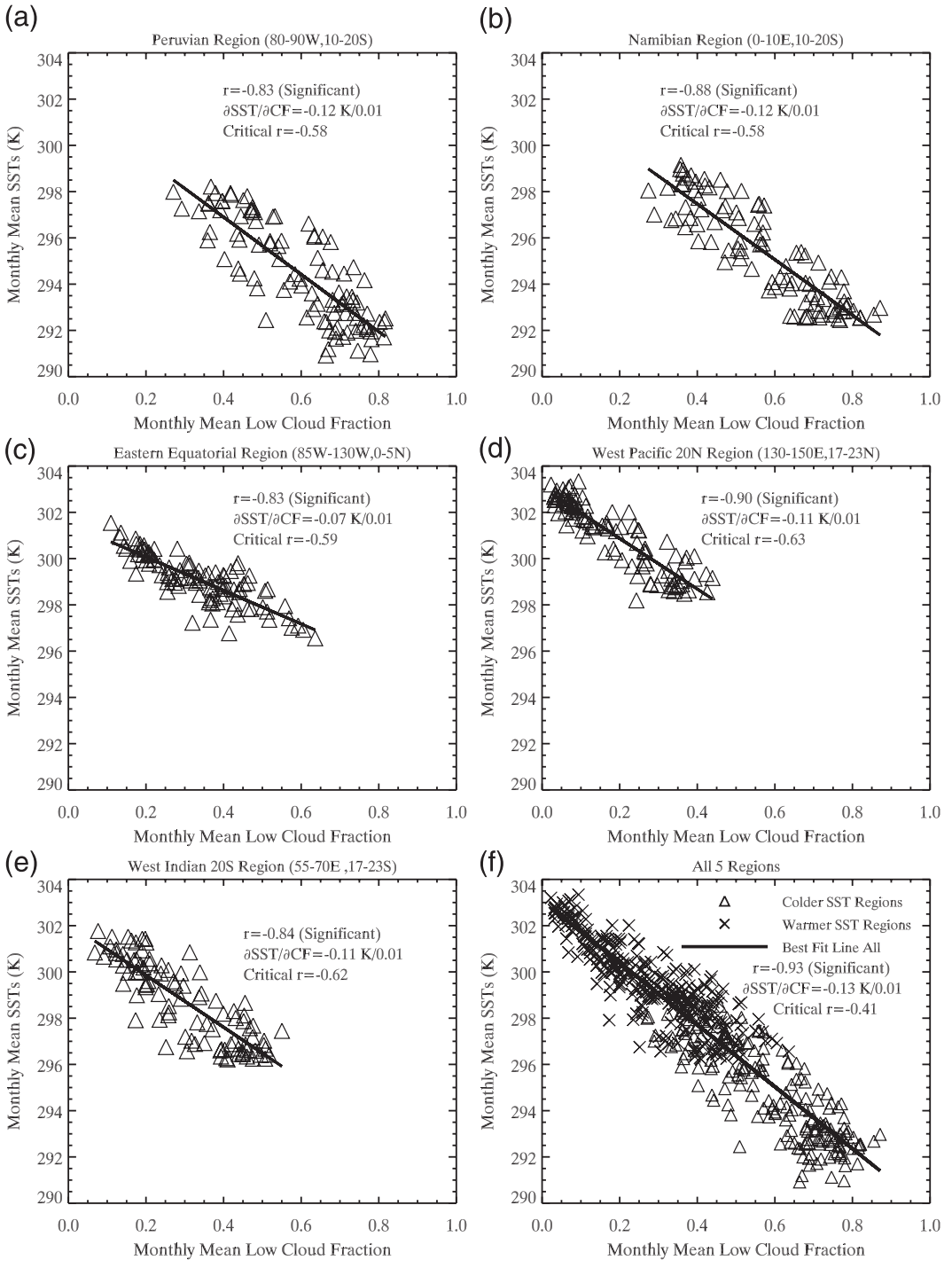


FIG. 6. Monthly mean SST vs LCF for the (a) Peruvian region, (b) Namibian region, (c) eastern equatorial region, (d) west Pacific ~20°N, (e) west Indian Ocean ~20°S, and (f) all five regions. Included are correlation coefficients, significant $r$ at the 99% level, and ΔLCF/ΔSST. Mean ΔSST/ΔLCF = −0.13 K/0.01.

(17°–23°N, 130°–150°E), and west Indian Ocean ~20°S (17°–23°S, 55°–70°E). These regions are highlighted as filled white boxes in Fig. 5f. We select all regions to provide a broad distribution of tropical/subtropical SST regimes where low cloud/SST patterns are closely intertwined. Scatterplots of monthly mean SST against LCF averaged within each subdomain are shown in Fig. 6 along with the correlation coefficients and ΔSST/ΔLCF.

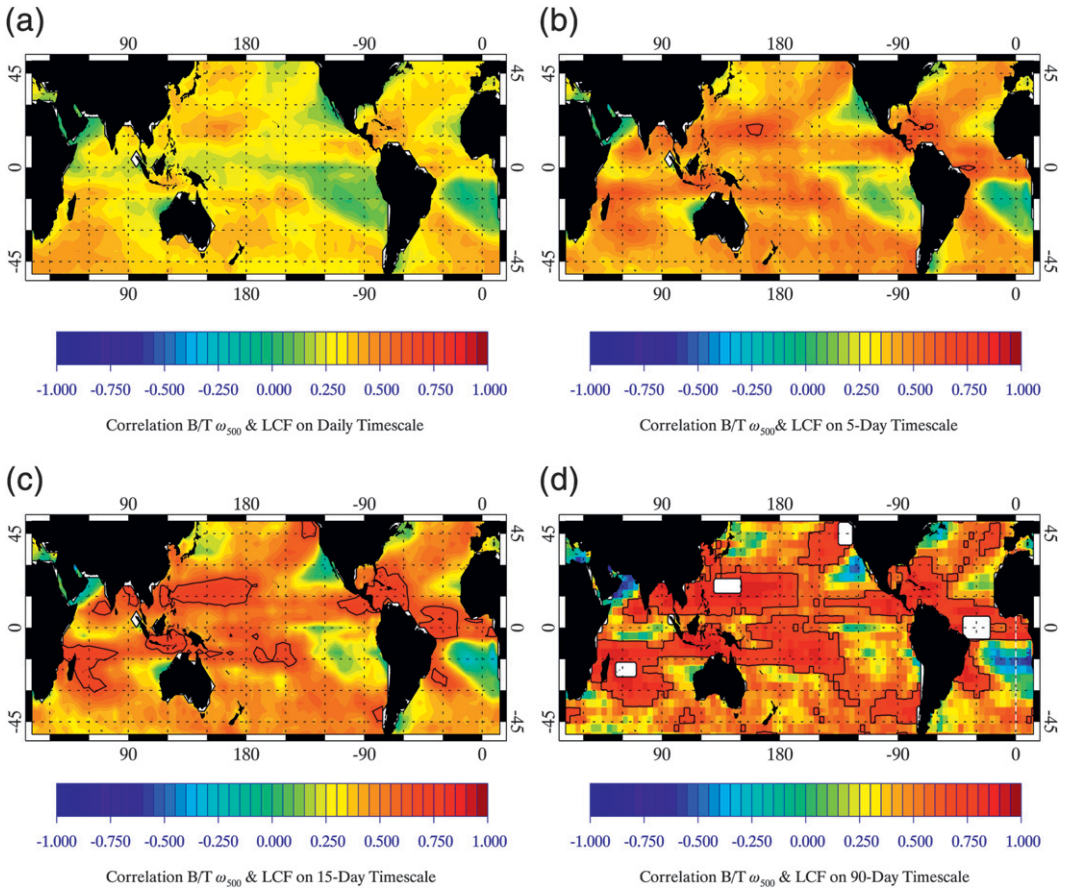


FIG. 7. Correlations between $\omega_{500}$ and LCF on (a) daily scale, (b) 5-day running mean, (c) 15-day running mean, and (d) 90-day running mean. Black contour values represent $r > 0.7$. White boxes in (d) are specific regions analyzed in Fig. 8.

The slopes in all regions are somewhat similar, though the eastern equatorial Pacific region has a smaller slope; it is also worth noting that SST minima lead LCF maxima in this region. The west Pacific region at ~20°N has the highest SSTs and, even though LCF is smaller, it is still tightly coupled to SST. While SST/LCF relationships differ slightly across the five selected regions, SST explains 86% of the monthly low-cloud variance ($r = -0.93$), as shown in Fig. 6f, with an overall five-region slope of $\Delta SST/\Delta LCF = -0.13$ K/0.01. The tight fit in the aggregate plot (Fig. 6f) suggests a nearly universal relationship in these lower-latitude regions. Qualitatively, this is similar to Bony et al. (1997), in which cloud fraction (tops primarily below the 600-hPa level for SSTs $< 299$ K) decreases with SST, though the slopes are somewhat more regime dependent in that study as cloud fraction drops off more quickly with SST in the stongest subsidence regime.

We next perform a correlation analysis of LCF with $\omega_{500}$ in an analogous way as for SST in which we examine the relationships as a function of time scale, explicitly for daily, 5-day, 15-day, and 90-day correlations (Fig. 7). As with SST, correlations between LCF and $\omega_{500}$ are relatively weak at the daily time scale albeit positive in most areas, except near zero in the vicinity surrounding the Peruvian and Namibian stratocumulus regions, off the coast of California/Baja California, and along the equator. Correlations become much more pronounced with 15-day averaging, particularly in the west Pacific near 20°N, western equatorial Atlantic, west Indian Ocean near 20°S, and even the northeast Pacific off the coasts of Washington and Oregon. With 90-day averaging these correlations become stronger and expand significantly in areal coverage, with large regions of correlation coefficients exceeding 0.70. Only a few regions show weak or even negative correlations between LCF and $\omega_{500}$, such as off the California/Baja California coasts and also across much of the eastern Atlantic along ~20°S. These regions are under the influence of large-scale subsidence year-round, and close examination reveals that stronger subsidence in these areas may inhibit low cloud formation, especially if the boundary layer cannot deepen above the lifting condensation level (Wood 2012; Randall and Suarez 1984). On the other hand, in many

low-latitude regimes that have a pronounced annual cycle of ascent and descent corresponding to the annual cycle of deeper convection, or the midlatitudes where the wintertime storm track is replaced by large-scale summertime highs, LCF tracks $\omega_{500}$ quite closely, especially for longer running means. To some extent LCF follows $\omega_{500}$ even on synoptic time scales, though other factors are likely important for shorter time scales as well, which may be beyond the scope of this study.

As examined with SST, in Fig. 8 we look at the individual monthly mean statistics for several regions with high LCF/$\omega_{500}$ correlations and include two regions analyzed before (west Pacific ~20°N and west Indian Ocean ~20°S) as well as the equatorial Atlantic (5°S–5°N, 20°–40°W) and North Pacific (40°–50°N, 125°–135°W), highlighted in white in Fig. 7d. The latter region allows a closer assessment of the midlatitudes off the Pacific Northwest coast. Scatterplots are shown for all 96 months for each of these four regions, including the least squares exponential lines and correlation coefficients. An exponential fit explains low cloud variance very well in each of the regions. Particularly in the west Pacific ~20°N, west Indian Ocean ~20°S, and North Pacific, a shift is apparent from LCF slowly increasing with $\omega_{500}$ to much more abrupt increases as $\omega_{500} > 0$. We aggregate all four regions in Fig. 8e with one best-fit curve, which has somewhat more scatter and a slightly lower correlation coefficient ($r = 0.86$) than the regions individually (ranging from 0.88 to 0.93) as the North Pacific has a smaller slope than the lower-latitude regions. A nontrivial amount of low cloud is observed over the North Pacific during months of ascent, which could potentially be bad-weather stratus as described in Norris (1998b) and associated with mean ascent as shown in Norris and Klein (2000).

All regions encompass plenty of months with mean ascent, and some a wide range of $\omega_{500}$, especially the North Pacific, which is in the heart of the storm track during winter but contains abundant isolated low clouds during summer. To better see this, we also plot the 3-month running mean LCF and $\omega_{500}$ time series for the North Pacific (Fig. 8f) and see pronounced summertime peaks (middle of each year) of both low clouds and $\omega_{500}$ with considerable interannual variability. During summer 2010, for instance, both the subsidence rate and LCF were particularly high.

Finally, while the strong increase of LCF with omega as omega becomes positive may be somewhat fortuitous, EIS also tends to vary exponentially with omega, with a strong increase starting around $\omega_{500} \sim 0$ Pa s$^{-1}$, though the EIS/$\omega_{500}$ relationship is more linear in the North Pacific (LTS and $\omega_{500}$ are slightly better correlated). These relationships indicate the level of connectedness between low-level stability and the large-scale circulation in these regions.

### c. Correlation versus time-scale synthesis

We synthesize correlation analyses by assessing the correlation between LCF and both SST and $\omega_{500}$ as a function of time scale for each of the above analyzed regions. For LCF/SST connections, correlations sharply increase with time from one day to approximately 2 weeks, then nearly horizontally asymptote at their maximum correlation coefficient after that point (Fig. 9a). The $x$ axis, which represents averaging time scale, is expanded between 1 and 30 days to show more detail during this shorter time period.

Analagous correlation coefficients as a function of running-day mean are shown in Fig. 9b, but now for $\omega_{500}$. The equatorial Atlantic region stands out with the largest correlation coefficients at all time scales though, as with SST, correlations in all regions increase most quickly at first, level off, and then only marginally increase beyond. In Table 1, the number of running mean days is shown for each of the regions to reach 90% of the 90-day correlation coefficient value. The range is 8–14 days for LCF/SSTs, and 10–28 days for LCF/$\omega_{500}$. Daily correlation values are also shown, with the largest negative LCF/SST $r$ value −0.67 (west Pacific ~20°N) and largest positive daily LCF/$\omega_{500}$ $r = 0.66$ over the equatorial Atlantic.

To quantify statistical significance of these correlations versus the number of running mean days, we have used the procedure described in detail in Bretherton et al. (1999), with an effective sample size calculated for each region versus the running mean day number based on the following formulation:

$$T_{xy} = T\left[\frac{1 - r_1 r_2}{1 + r_1 r_2}\right] \tag{4}$$

in which $r_1$ and $r_2$ are the lag-one autocorrelations and $T$ the size of the time series. Then $T_{xy}$ is used to calculate the critical correlation coefficient that must be exceeded at the 99% confidence level for the correlation at a particular running-mean day number to be significant. Using this test, all correlation coefficients at all averaging time scales are statistically significant at the 99% confidence level, shown as thin lines in Fig. 9.

With regards to a better interpretation of Fig. 9a, appreciable SST changes occur at a much slower temporal scale compared to clouds, which have a rather large synoptic variability. When synoptic scales are filtered out (averaging multiple days to a few weeks), LCF/SST correlations increase dramatically as the

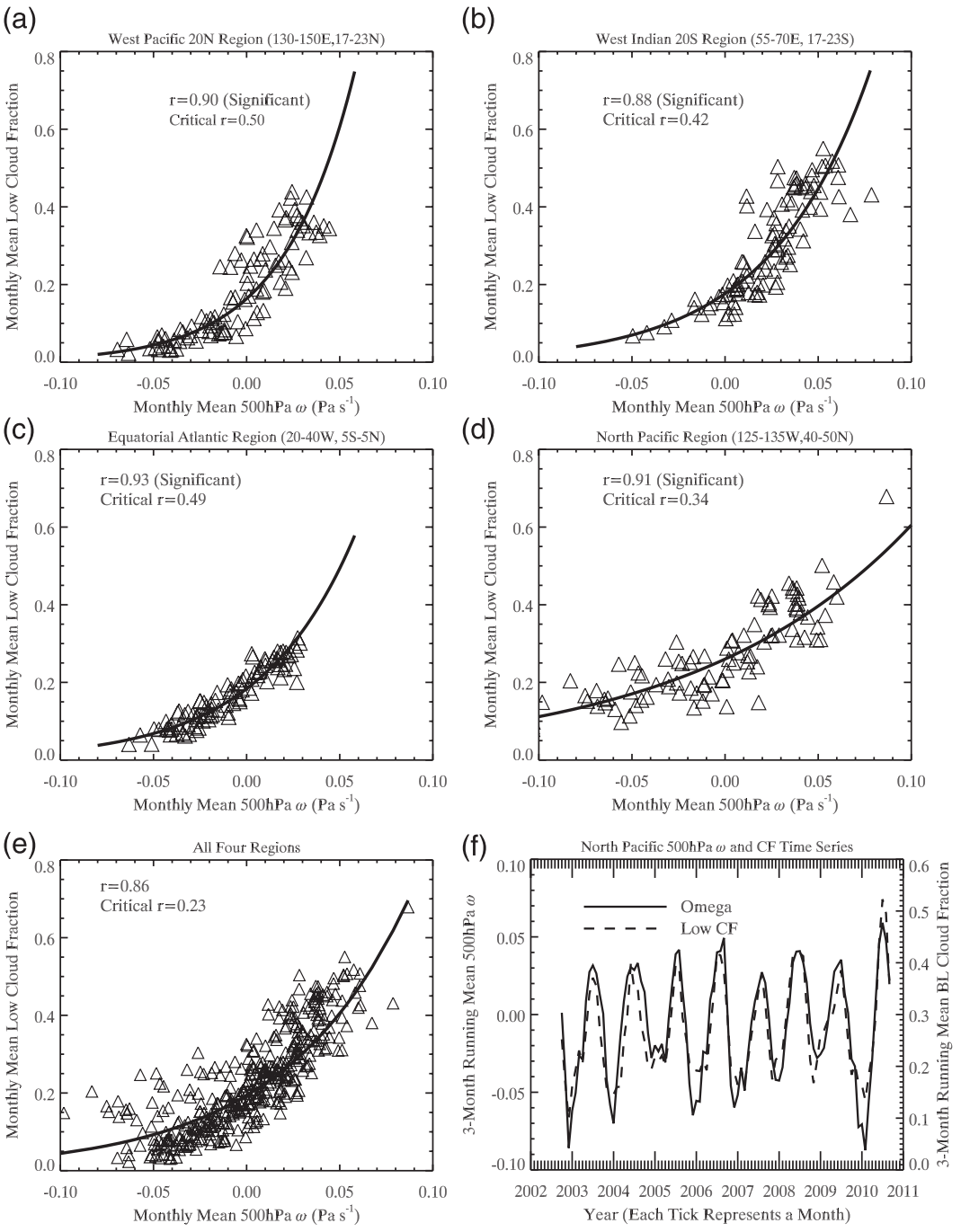


FIG. 8. Monthly mean LCF vs $\omega_{500}$ for (a) west Pacific ~20°N, (b) west Indian Ocean ~20°S, (c) equatorial Atlantic, (d) North Pacific, and (e) all four regions. All regions have best exponential fits and significant $r$ at the 99% level. (f) Three-month running mean $\omega_{500}$ and LCF time series for the North Pacific.

annual cycle is approached. Vertical velocity has correspondingly much higher synoptic variability, but is still much more weakly correlated with LCF at very short time scales. Indeed, the variance of clouds is much larger at short time scales compared to longer time scales, but as Klein (1997) points out, random effects may be at play as well, which are suppressed when more days are averaged together. As an aside, averaging over a larger area (4° × 4° boxes) also yields higher short-term correlations than the maximum of $r = 0.35$ in Klein (1997) (for the most correlated variables: cold advection or stability) for one point (30°N, 140°W).

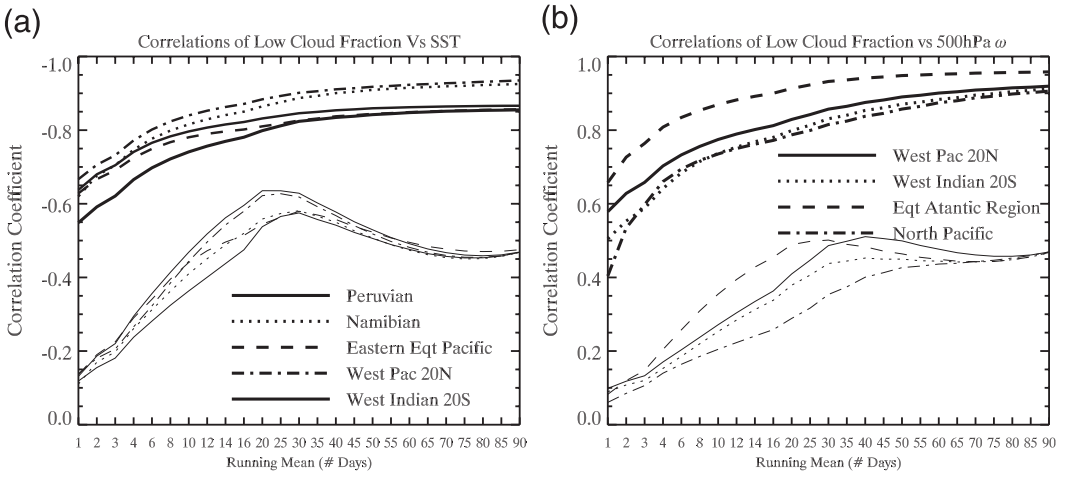


FIG. 9. Correlation coefficients as a function of number of running mean days for (a) LCF vs SST and (b) LCF vs $\omega_{500}$ for each of the regions as defined in the text (thick lines). Also shown are critical $r$ values for each region as a function of running mean day in the same line style but thin lines at the 99% confidence level. Details are explained in the manuscript.

### *d. Monthly correlation maps of LCF with SST, ω, advection, LTS, EIS, and 700 hPa temperature*

We summarize section 4 by examining monthly correlations of not only the variables already tested, but also surface advection and stability parameters (LTS and EIS). As mentioned in the introduction, a number of previous studies have quantified strong correlations between low cloud cover/LTS (Klein and Hartmann 1993) and EIS (Wood and Bretherton 2006), but here spatial correlation patterns are shown of these variables (not anomalies), which have been less appreciated.

Figures 10a,b underscore correlation patterns very similar to the longer running-mean correlation maps in Figs. 5 and 7, with some rather subtle differences. For example, strong LCF/SST correlations extend farther poleward over the far western Pacific compared to Fig. 5c or 5d. In Fig. 10c, LCF and surface cold advection are generally positively correlated, particularly near Ocean Weather Station November (30°N, 140°W) as analyzed by Klein (1997). Cold advection is also coupled to LCF over the far western Pacific and just offshore of northeast North America; during boreal winter cold-air outbreaks with northerly/northwesterly cold continental air circulation around the continental high over a warm sea surface destabilize the boundary layer and can cause shallow convection (Li 1994). In this region (especially the far west Pacific), LTS is strongly *negatively* correlated with LCF (Fig. 10d) and EIS weakly *positively* so (Fig. 10e).

In general, correlation patterns between both LCF/LTS and LCF/EIS are rather similar to those of LCF/−SST

TABLE 1. Daily correlation coefficient and time (days) for correlation coefficient to reach 90% of 90-day running mean value, and day of year of minimum SST, maximum LCF, and maximum $\omega_{500}$.

| LCF/SST region | Daily LCF/SST correlation coefficient | Days to reach 90% of 90-day value | Day of year of minimum SST | Day of year of maximum LCF |
|---|---|---|---|---|
| Peruvian | −0.55 | 14 | 261 | 242 |
| Namibian | −0.61 | 14 | 257 | 242 |
| Eastern equatorial Pacific | −0.64 | 10 | 282 | 302 |
| West Pacific ~20°N | −0.67 | 12 | 44 | 31 |
| West Indian Ocean ~20°S | −0.51 | 8 | 243 | 218 |

| LCF/$\omega_{500}$ region | Daily LCF/$\omega_{500}$ correlation coefficient | Days to reach 90% of 90-day value | Day of year of maximum $\omega_{500}$ | Day of year of maximum LCF |
|---|---|---|---|---|
| West Pacific ~20°N | 0.58 | 20 | 45 | 31 |
| West Indian Ocean ~20°S | 0.51 | 28 | 220 | 218 |
| Equatorial Atlantic | 0.66 | 10 | 268 | 259 |
| North Pacific | 0.46 | 26 | 194 | 200 |

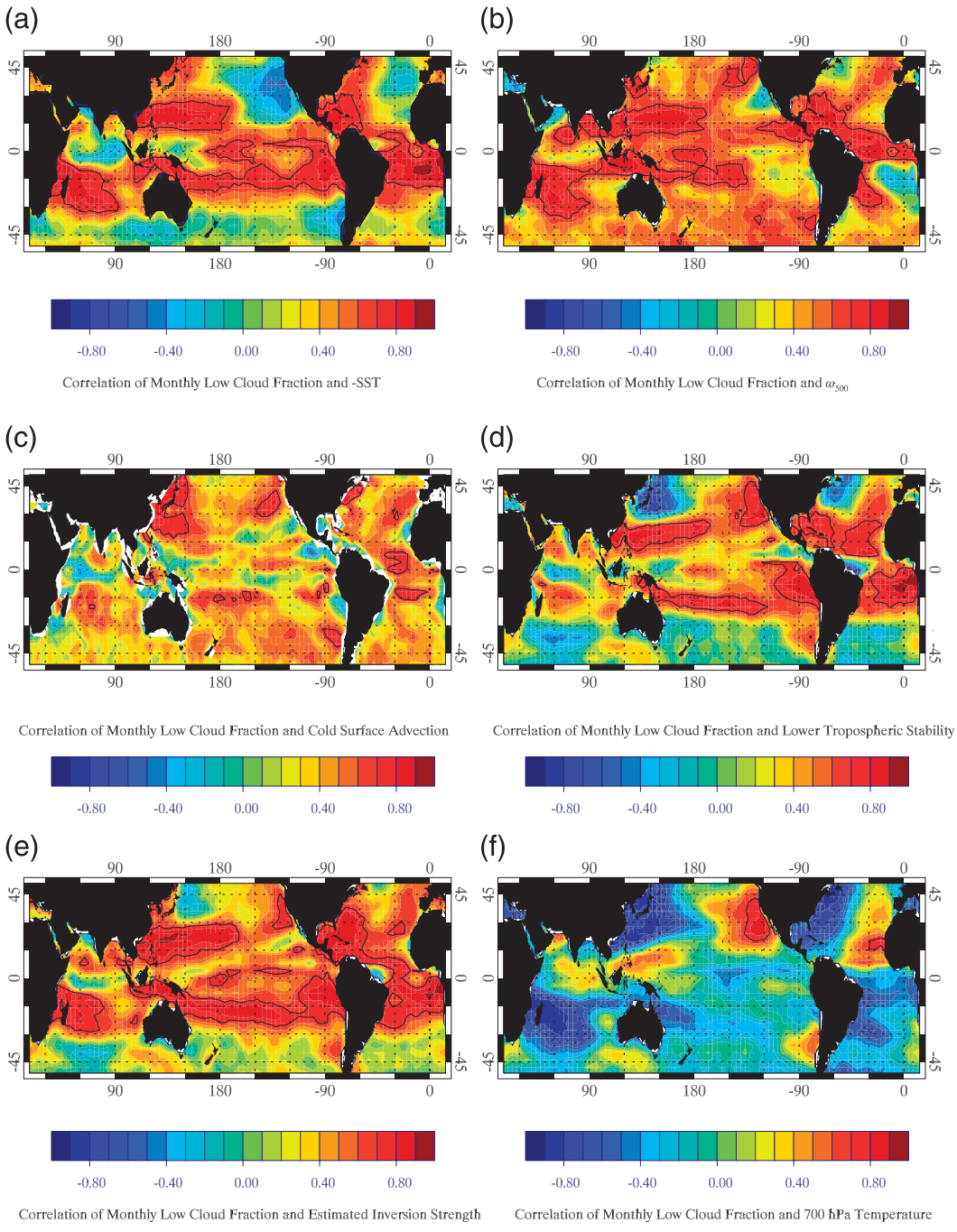


FIG. 10. Monthly mean correlations between LCF and (a) −SST, (b) $\omega_{500}$, (c) cold surface advection, (d) LTS, (e) EIS, and (f) $T_{700}$. Solid contours indicate $r > 0.7$; dashed contours $r < -0.7$.

except that both LTS and EIS are strongly positively correlated with the northeast Pacific and northeast Atlantic, regions where LCF is out of phase with minimum SST (explained more in section 5) but, instead, in phase with 700-hPa temperature (Fig. 10e). Aside from these regions, Figs. 10a,d,e look rather similar to each other, though LCF/EIS correlations are stronger than LCF/LTS correlations. Regions where the correlations are similar to SST suggest that EIS (or LTS) is largely driven by SST; EIS and −SST are strongly positively correlated with each other across the latitudes, especially between 30°S and 30°N and all western ocean basins (extending far poleward), though we do not explicitly show this and save this analysis for future work. Finally, Fig. 10e shows

monthly correlations between LCF and the 700-hPa temperature, which shows strong correlations off the west coast of North America, indicating that stability in these regions is largely free-troposphere driven, warranting futher investigation.

## 5. Annual cycle of SST, $\omega_{500}$, and LCF

### *a. Oceanic analysis between 50°S and 50°N*

We next turn to the assessment of the annual cycle of SST, $\omega_{500}$, and LCF following the procedure described in section 3. The annual cycle of each of the variables within each $4° \times 4°$ box is from an 8-yr climatology, and from this we calculate the phase of the annual harmonics of minimum SST, maximum $\omega_{500}$, and maximum LCF. We also have performed an annual cycle analysis of LTS and EIS, but in the interest of space leave these details for future work. If the fraction of variance explained by the annual cycle is less than 0.3, we select the middle day of the 30-day minimum/maximum periods for phase information. In cases where the annual harmonic amplitude (maximum minus mean) of LCF is less than 0.05, or $\omega_{500}$ is less than 0.01 Pa $s^{-1}$, we neglect analysis of the phase and, thus, do not compute lead/lag relationships between LCF and SST or LCF and $\omega_{500}$. Harmonic analysis is performed objectively everywhere else. In Fig. 11, we show the contours of the month of the annual harmonic of minimum SST (Fig. 11a), month of maximum LCF (Fig. 11b), phase difference in days of maximum LCF and minimum SST (Fig. 11c) with LCF leading denoted by positive values, fraction of SST variance explained by the annual harmonic (Fig. 11d), and fraction of LCF variance explained by the annual harmonic (Fig. 11e). Largely following the annual cycle of insolation with some lag, minimum SSTs in the Northern Hemisphere occur during the first few months of the year and largely between August and September in the Southern Hemisphere. Away from low latitudes, SSTs generally are at a minimum a few months after the hemispheric winter solstice, owing to the large heat capacity of the ocean, although winds and ocean circulations play a role in horizontal gradients as well. Near the equator along the Pacific, the eastern Pacific minimum SSTs occur at least one to two months earlier than in the western Pacific equatorial warm region. Furthermore, a semiannual SST harmonic explains a considerable fraction of variance (more than 50%, not shown) near the equator in the central Pacific and equatorial and northern Indian Ocean regions, which is physically consistent with the semiannual cycle in insolation over the low latitudes (e.g., Kessler et al. 1998). Cloud cover transforms an expected semiannual SST cycle in the eastern Pacific into an annual one (Kessler et al. 1998).

In our analysis, where the maximum low-cloud phase is assessed, maximum LCF occurs during months $9 \sim 10$ in the far eastern equatorial Pacific, and later in the year or the beginning of the year farther west. The phase of maximum LCF looks qualitatively similar to SST in the Southern Hemisphere where the fraction of variance explained is high, though, on the whole, low-cloud maxima tend to lead SST minima by at least 10–15 days or more. In the western Pacific region near ~20°N discussed earlier, the fraction of variance of LCF explained by the annual harmonic is high and the timing of maximum LCF is also ahead of minimum SST. In the eastern Pacific subtropics and northern and northeastern Pacific, however, SSTs reach their minima during late winter, but LCF peaks during late spring or summer depending on location. Coincidentally, maximum LTS/EIS in the north and eastern Pacific is more closely in phase with LCF, largely when free tropospheric temperature is warmest, and EIS and LCF are in phase over the northwestern Pacific (not shown), though LTS is anticorrelated with LCF there. Except over the warm pool regions discussed earlier, the annual SST harmonic is dominant globally, with the fraction of variance explained exceeding ~80% in most locations. Finally, the fraction of LCF variance explained by the annual harmonic is high in many low-latitude regions in both hemispheres, as well as the northeastern Pacific extending up to the midlatitudes. Over the equatorial western and central Pacific, deep convection is dominant, with few isolated low-topped clouds, and thus the LCF fraction of variance explained by the annual harmonic is low.

We next present, in Fig. 12, an analogous analysis but for $\omega_{500}$ and lead/lag LCF–$\omega_{500}$ relationships. As with minimum SSTs, the phasing of maximum $\omega_{500}$ in the subtropical western Pacific occurs early in the year, though in the North Pacific region analyzed before, maximum $\omega_{500}$ occurs during the middle of boreal summer. Over the equatorial eastern Pacific and equatorial Atlantic, maximum $\omega_{500}$ broadly follows the timing of minimum SST (Figs. 11a and 12a), and generally clouds tend to be in approximate phase with $\omega_{500}$ in the Southern Hemisphere low latitudes. The mapping of maximum $\omega_{500}$ is considerably more noisy than that of minimum SST, but in areas where the fraction of variance explained by the annual $\omega_{500}$ harmonic is high (Fig. 12d), LCF generally slightly leads $\omega_{500}$ in the subtropical western Pacific and $\omega_{500}$ leads LCF slightly in most of the Southern Hemisphere. The observation of the phasing differences generally being small in regions where the annual cycle is well defined is consistent with the notion of clouds responding more quickly to free-tropospheric dynamics. We hone in more carefully on specific regions in section 5b.

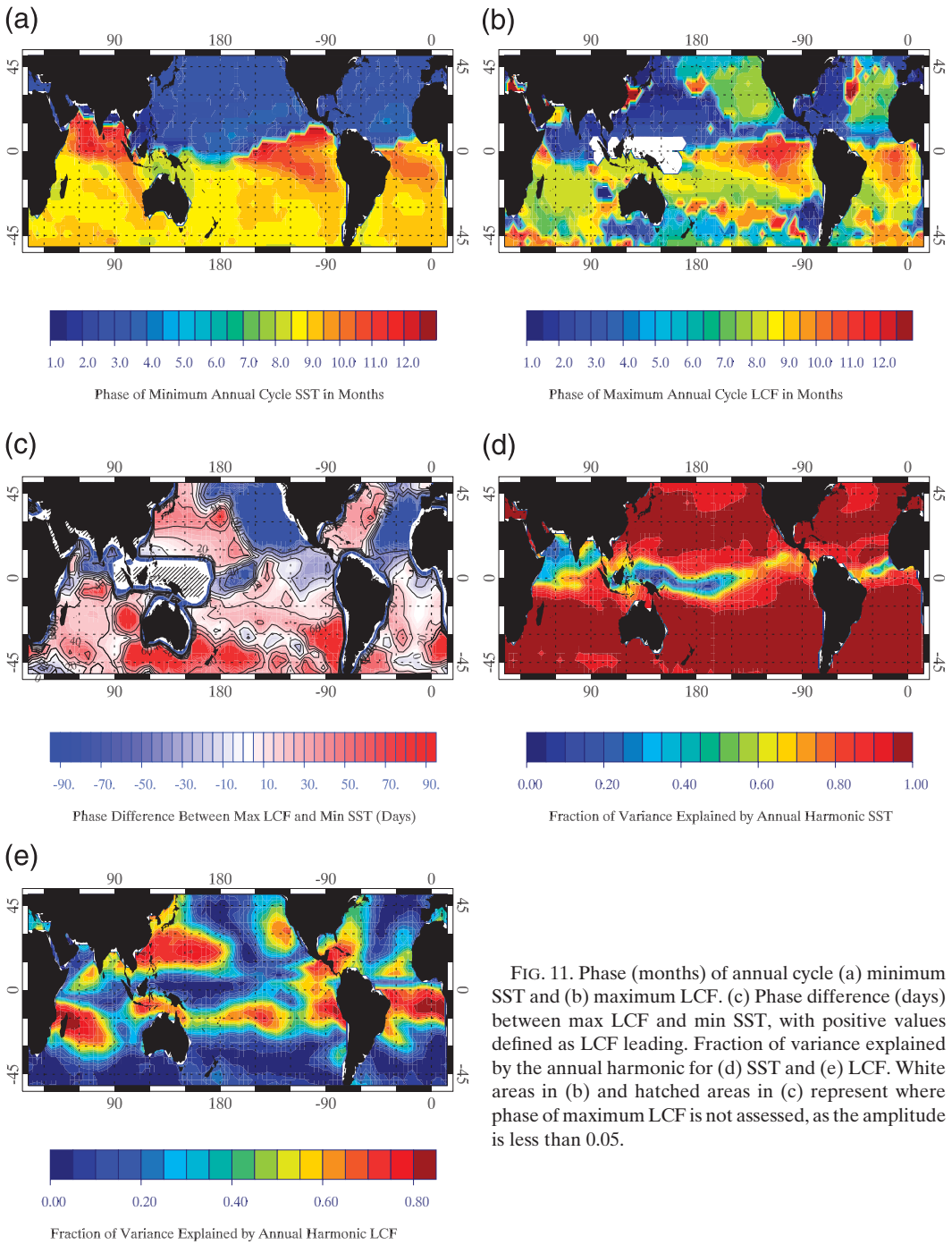


FIG. 11. Phase (months) of annual cycle (a) minimum SST and (b) maximum LCF. (c) Phase difference (days) between max LCF and min SST, with positive values defined as LCF leading. Fraction of variance explained by the annual harmonic for (d) SST and (e) LCF. White areas in (b) and hatched areas in (c) represent where phase of maximum LCF is not assessed, as the amplitude is less than 0.05.

In the expansive subsidence regions of the southeastern Pacific (extending to the equatorial cold tongue) and Atlantic, the $\omega_{500}$ annual cycle is nearly nonexistent—regions nearly always under mean subsidence. The lack of a clear annual cycle of $\omega_{500}$ does not preclude subseasonal or synoptic $\omega_{500}$ variations that may still be coherent with low-cloud organization and patterns—an active area of recent (Xu et al. 2005; George and Wood 2010) and current research. Finally, in the low latitudes, the $\omega_{500}$ annual cycle amplitude (not shown) and fraction of variance explained are largest over the convective margins or even the edge of the ITCZ—regions with seasonal migrations of subsidence and ascent.

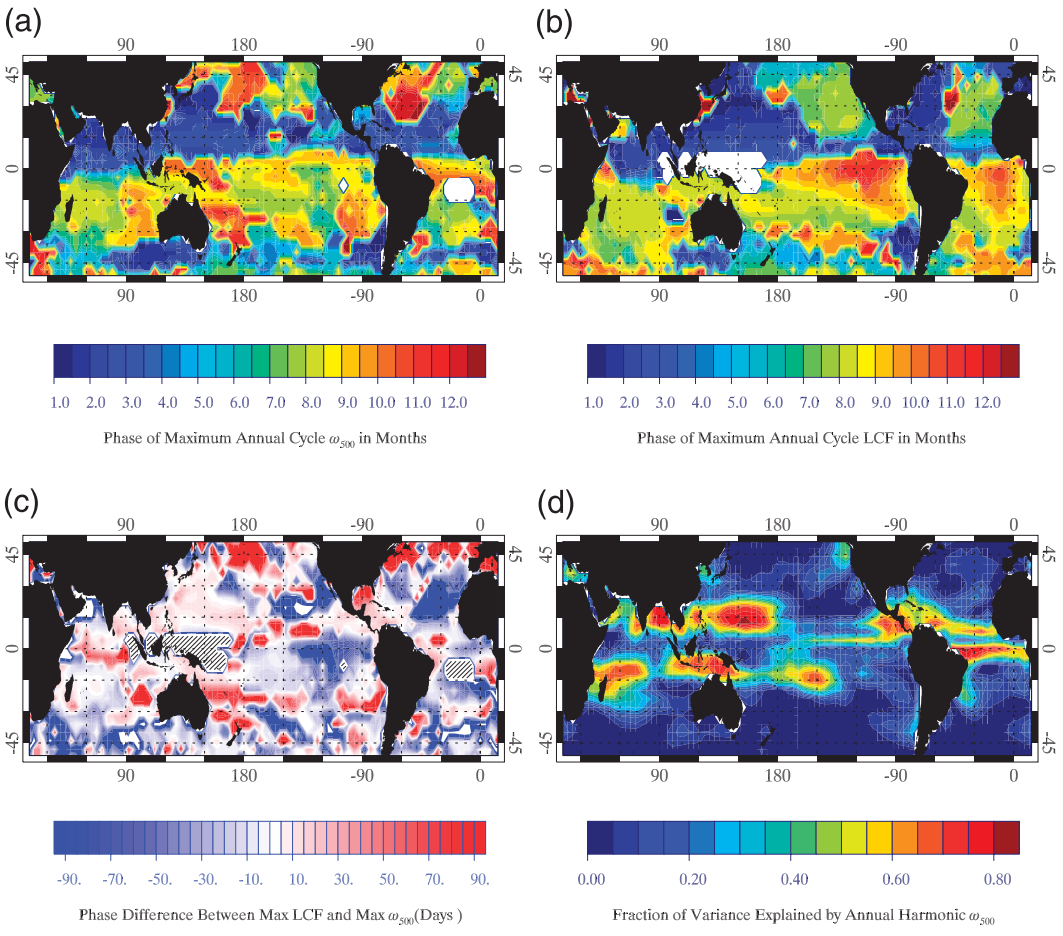


FIG. 12. (a) Phase (months) of annual cycle maximum $\omega_{500}$. (b) As in Fig. 11b. (c) Phase difference (days) between max LCF and max $\omega_{500}$, with positive values defined as LCF leading. (d) Fraction of variance explained by the $\omega_{500}$ annual harmonic.

### *b. Annual cycle of specific regions*

We now examine the annual cycle of SST, $\omega_{500}$, and clouds in the specific subdomains analyzed earlier to more carefully assess phasing differences. The fractional variance explained by the annual harmonic of SSTs is high in all regions, ranging from 0.85 over the Southern Hemisphere equatorial Atlantic to 0.99 over the west Indian Ocean at ~20°S, and the fractional variance explained by the annual LCF harmonic is at least 0.50. In the regions with strong $\omega_{500}$/LCF correlations, the fractional variance explained by the annual $\omega_{500}$ harmonic is also fairly high, with the Southern Hemisphere equatorial Atlantic at 0.74, though less so over, for instance, the west Indian Ocean at ~20°S (0.45) and the North Pacific (0.39), where considerable synoptic variability exists associated with the storm track and baroclinic frontal systems: nevertheless, the $\omega_{500}$ annual cycle is dominant above higher frequency modes.

In Figs. 13a–e, we show the 8-yr daily climatology of SSTs (thin solid) and LCF (thin dashed) as well as the annual harmonic sinusoid curves for SSTs (thick solid) and clouds (thick dashed). In all regions, the sinusoid curves visually fit the observed daily curves rather well. For reference, based on the annual harmonic curve, the day of minimum SST and maximum LCF for each region are also shown. Except for the eastern equatorial Pacific where the minimum annual harmonic SSTs lead maximum LCF by ~20 days (though visual inspection shows an imperfect fit of the phasing of minimum SSTs with the harmonic), in most regions maximum cloud amount leads minimum SSTs by 20 days or more, albeit less (~13 days) in the west Pacific ~20°N. Considerable day-to-day variability of clouds during the season of maximum cloud amount exists (boreal winter and early spring), which is not driven purely by SST variations that change on a much slower time scale than clouds. In the Peruvian region, clouds lead minimum SSTs by almost 20 days, which is consistent with the analysis by Takahashi (2005) in which maximum cloud albedo off the coast of Peru was generally found to lead minimum

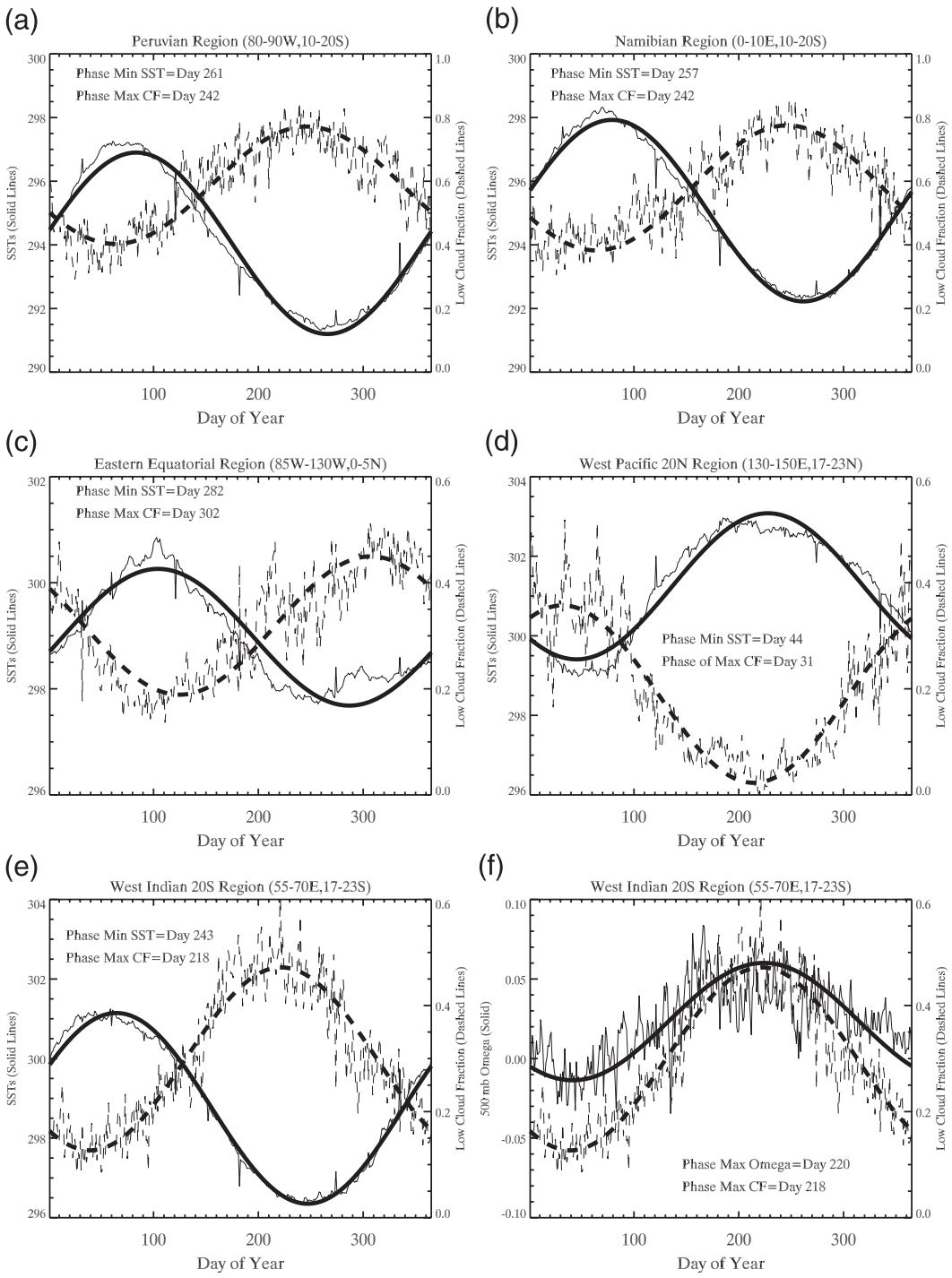


FIG. 13. An 8-yr SST (thin solid) and LCF (thin dashed) climatologies with annual harmonics (SSTs: thick solid, LCF: thick dashed) for (a) Peruvian, (b) Namibian, (c) eastern equatorial region, (d) west Pacific ~20°N, and (e) west Indian Ocean ~20°S regions. (f) 8-yr $\omega_{500}$ (solid) and LCF (dashed). Phases in days are also given.

SSTs by 20–30 days. The peak of maximum albedo of that study is mid to late August, consistent with our peak in this study of day 242, the very end of August. The notion of clouds amplifying the SST annual cycle in this region is physically logical. We also examined the phasing of SFC_TEMP_ADV (not shown) and cold advection peaks before maximum LCF and minimum SST, also consistent with the analysis by Takahashi. The SST

and LCF annual cycles are nearly identical in the Namibian region, suggesting similar forcing and circulation in the southeast Atlantic to the southeast Pacific.

Finally, we perform annual cycle $\omega_{500}$ and LCF analyses over the west Pacific ~20°N, the west Indian Ocean ~20°S, the Southern Hemisphere equatorial Atlantic (same longitude as equatorial Atlantic), and the North Pacific but, rather than show all regions, we only show the west Indian Ocean ~20°S in Fig. 14f, and report the harmonic maximum day of $\omega_{500}$ and LCF in Table 1 for the other regions. Except over the west Pacific ~20°N, where LCF leads $\omega_{500}$ by ~14 days, LCF and $\omega_{500}$ are nearly in phase in the other three locations, with an offset of only 2 days over the west Indian Ocean ~20°S. Also, in the North Pacific, the annual harmonic $\omega_{500}$ peak occurs in the middle of July (only six days before the annual harmonic LCF peak), though a broad subsidence maximum occurs from late spring through late summer, and understanding shorter-term variability of LCF in this region would require a more careful subseasonal analysis.

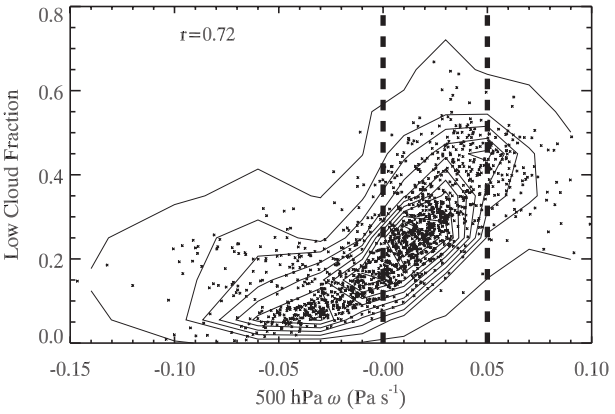


FIG. 14. LCF vs $\omega_{500}$ from 8-yr daily climatology cloud and $\omega_{500}$ from the four regions analyzed in Fig. 8, including the west Pacific ~20°N, west Indian Ocean ~20°S, equatorial Atlantic, and North Pacific. Thin contour lines are for LCF/omega bins with under 0.05 of data, and thicker contours for bins with more than 0.05 of total data. Thick dashed lines represent $\omega_{500}$ values of 0.0 and 0.05 Pa $s^{-1}$.

## 6. Discussion and summary

In this study we have used 8 yr of daily gridded MODIS level-3 cloud data and corresponding ERA-Interim output of large-scale dynamics to investigate relationships of low-topped clouds with SSTs/atmospheric dynamics, as a function of both location and time scale. Our screening process helps ensure the analysis of 1° × 1° grids containing clouds with tops either warmer than 270 K and pressures greater than 500 hPa, or more homogeneous scenes with tops below 4 km. We have furthermore assessed annual cycle characteristics of low-topped cloud cover (LCF), SSTs, and $\omega_{500}$ to quantitatively assess not only the ability of the annual cycle to explain the variance, but also lead/lag relationships as they relate to cloud and dynamical feedbacks. The primary findings of this study are as follows.

1) LCF is strongly anticorrelated with SST over low latitudes, with the correlation coefficient between LCF and −SST exceeding 0.70 in 56% of oceanic regions between 25°S and 25°N with a 90-day running mean. Correlations between LCF and −SST increase with averaging time scale especially between 1 and 15 days, reaching 90% of their 90-day values between 8 and 14 days, which is likely linked to averaging out synoptic variability of clouds compared to the much slower time scale of SST changes in which the annual cycle is dominant. Weak correlation regions include the western Pacific and Indian warm pool regions as well as the northeastern Pacific. The northeastern Pacific LCF is more connected to both the strength and location of the remote Pacific high pressure center as well as the free-tropospheric temperature, the latter of which (temperature at 700 hPa) is much more closely connected than SSTs to low-level stability in that region.
2) LCF is strongly correlated with $\omega_{500}$ at most locations, with a global $r = 0.55$ between 50°S and 50°N (with a 90-day running mean), and over one-third of locations with $r > 0.70$. Strong correlations include midlatitude regions as well. Exceptions of strong LCF/$\omega_{500}$ correlations include the subtropical southeast Pacific/Atlantic and Californian stratocumulus regions—these regions are under mean subsidence year-round with a fairly small annual cycle. In the Californian stratus region, LCF generally increases with subsidence for $\omega_{500} < 0.05$ Pa $s^{-1}$, but then decreases for subsidence rates beyond, and monthly $\omega_{500}$ variance appears to correlate with LCF there; Namibian LCF weakly decreases with increasing subsidence.
3) Where the fraction of variance explained by the annual harmonic LCF is high, maximum LCF tends to lead minimum SST by ~15–30 days. This primarily occurs between 25°S and 25°N where EIS and LTS are SST dominated, and stability parameters also lag maximum LCF. This implies that low-topped clouds may possibly have the effect of amplifying the SST annual cycle. The long time scale of SST changes relative to the fast physics of cloud formation does not preclude internal feedbacks, especially since SSTs in these regions are controlling stability.
4) For monthly mean correlations, the fraction of oceanic areas between 50°S and 50°N with $|r| > 0.7$ is 0.27 for LCF/EIS, 0.24 for LCF/$\omega_{500}$, 0.224 for LCF/SST, 0.17 for LCF/LTS, and 0.07 for LCF/surface temperature advection. This indicates that EIS is a powerful predictor of isolated low-cloud amount. Within

certain regimes, however, SST, $\omega_{500}$, or even cold advection may be slightly stronger predictors.

In five specific regions assessed with strong anticorrelations between SSTs and LCF, $r = -0.93$, $\Delta$SST/$\Delta$LCF $= -0.13$ K/0.01, and $r = 0.90$ between EIS and LCF. This includes two primary stratocumulus regimes, the eastern Pacific equatorial cold tongue region, and two lower-latitude regimes (near 20°S) with a clear annual cycle of ascent and descent—the west Pacific at ~20°N with the strongest ascent. Our results are in general agreement with previous studies examining low cloud fraction/SST relationships; Oreopoulos and Davies (1993) indicate a 3%–6% decrease of low clouds in the southeastern Pacific and Atlantic, Bony et al. (1997) a value of $-4\%$ K$^{-1}$, and Eitzen et al. (2011) $-3.44\%$ K$^{-1}$. We report the SST change per fractional LCF change since clouds lead SST minima in the regions assessed; calculating the best-fit line per degree SST instead gives an LCF change of close to $-6.5\%$ K$^{-1}$ for monthly means, and slightly less than $-6\%$ K$^{-1}$ for 8-yr daily climatology values. The latter is slightly lower since minimum SST lags LCF in all but one of five regions by less than one month. Our $\Delta$SST/$\Delta$LCF may also be somewhat larger than in Bony et al. (1997), as middle/higher clouds are not excluded in their analysis; in fact, mean cloud top pressure decreases strongly for SSTs $> 298$ K, reflecting the presence of higher clouds. Four of the five regions that we have analyzed have very similar slopes regardless of the SST range, pointing toward a more universal $\Delta$SST/$\Delta$LCF for isolated low clouds at lower latitudes. This has ramifications for a positive LCF feedback in low latitudes, particularly since EIS is tightly coupled to low clouds and SSTs in these regions.

Although our analysis of three low-latitude regions and one midlatitude region suggests that monthly LCF increases exponentially with monthly $\omega_{500}$ ($r = 0.86$ for all four regions combined), careful analysis of the *daily* LCF versus $\omega_{500}$ relationships (based on 8-yr daily climatologies) indicates that LCF begins leveling off at a subsidence rate close to 0.05 Pa s$^{-1}$ and even tends to decrease beyond this, suggesting a limit of the strong positive relationship between LCF and $\omega_{500}$ (Fig. 14, $r = 0.72$), perhaps through the effect of suppressing the inversion to a height too shallow to support boundary layer clouds. More work on this is poised for future studies. This limit may also help better explain the weaker positive or even very slight negative correlations in primary stratocumulus low cloud regimes whose free circulation is nearly always subsiding; Eitzen et al. (2011) also shows that subsidence strength in mean subsidence regions is not a major determinant of low clouds. Current work under way for the southeast Pacific, extending out to the date line, suggests that monthly $1° \times 1°$ LCF is tightly coupled to $\omega_{500}$ (for two months of data), with a strong increase starting at $\omega_{500} \sim 0$ Pa s$^{-1}$ to ~0.05 Pa s$^{-1}$, after which point a drop-off in both LCF and cloud water path is observed for very strong subsidence rates.

Studies examining $2 \times CO_2$ simulations (e.g., Williams et al. 2006) have demonstrated a projected weakening of the Hadley circulation, which would weaken $\omega_{500}$ in the subtropics, and also would tend to reduce LCF even in the primary stratocumulus regions that we analyzed because of weaker remote forcing (e.g., weaker trade winds, cold advection), though this signal is less clear in the southeastern Atlantic where we observe a slight negative correlation between vertical velocity and LCF. Examination of regime changes would be important as well; a weakening of the large-scale circulation in current moderate subsidence regimes may be a strong positive low-cloud feedback with global warming since isolated low clouds in those areas tend to be more sensitive to $\omega_{500}$.

Finally, our emphasis on the observational and reanalysis-derived annual cycle of large-scale dynamics is important not only as a test bed for climate models for today's climate, but changes in characteristics of the annual cycle with climate warming, including amplitudes and phasing of SST, LTS/EIS, advection, and $\omega_{500}$, could have significant implications for annual cycle properties of low clouds, significant for low cloud feedbacks.

*Acknowledgments.* The authors wish to thank three anonymous reviewers for their thorough and constructive recommendations, which have greatly enhanced this manuscript. The research described in this paper was carried out at the Jet Propulsion Laboratory, California Institute of Technology, under a contract with the National Aeronautics and Space Administration.

## REFERENCES

Behrangi, A., T. Kubar, and B. Lambrigtsen, 2012: Phenomenological description of tropical clouds using *CloudSat* cloud classification. *Mon. Wea. Rev.,* in press.

Bony, S., K.-M. Lau, and Y. C. Sud, 1997: Sea surface temperature and large-scale circulation influences on tropical greenhouse effect and cloud radiative forcing. *J. Climate,* **10,** 2055–2077.

Bretherton, C. S., E. Klinker, A. K. Betts, and J. A. Coakley Jr., 1995: Comparison of ceilometer, satellite, and synoptic measurements of boundary layer cloudiness and the ECMWF diagnostic cloud parameterization scheme during ASTEX. *J. Atmos. Sci.,* **52,** 2736–2751.

——, M. Widmann, V. P. Dymnikov, J. M. Wallace, and I. Blade, 1999: The effective number of spatial degrees of freedom of a time-varying field. *J. Climate,* **12,** 1990–2009.

Dee, D. P., and Coauthors, 2011: The ERA-Interim reanalysis: Configuration and performance of the data assimilation system. *Quart. J. Roy. Meteor. Soc.,* **137,** 553–597, doi:10.1002/qj.828.

Eitzen, Z. A., K.-M. Xu, and T. Wong, 2008: Statistical analyses of satellite cloud object data from CERES. Part V: Relationships

between physical properties of marine boundary layer clouds. *J. Climate,* **21,** 6668–6688.

——, ——, and ——, 2011: An estimate of low-cloud feedbacks from variations of cloud radiative and physical properties with sea surface temperature on interannual time scales. *J. Climate,* **24,** 1106–1121.

George, R. C., and R. Wood, 2010: Subseasonal variability of low cloud radiative properties over the southeast Pacific Ocean. *Atmos. Chem. Phys.,* **10,** 4047–4063.

Greenwald, T. J., and S. A. Christopher, 1999: Daytime variation of marine stratocumulus microphysical properties as observed from geostationary satellite. *Geophys. Res. Lett.,* **26,** 1723–1726.

Hahn, C. J., S. G. Warren, J. London, R. L. Jenne, and R. M. Chervin, 1998: Climatological data for clouds over the globe from surface observations. Oak Ridge National Laboratory Rep. NDP-026, 54 pp.

Hubanks, P. A., M. D. King, S. Platnick, and R. Pincus, 2008: MODIS atmosphere L3 gridded product. MODIS Algorithm Theoretical Basis Doc. ATBD-MOD-08, 96 pp.

Kessler, W. S., L. M. Rothstein, and D. Chen, 1998: The annual cycle of SST in the eastern tropical Pacific, diagnosed in an ocean GCM. *J. Climate,* **11,** 777–799.

Klein, S. A., 1997: Synoptic variability of low-cloud properties and meteorological parameters in the subtropical trade wind boundary layer. *J. Climate,* **10,** 2018–2039.

——, and D. L. Hartmann, 1993: The seasonal cycle of low stratiform clouds. *J. Climate,* **6,** 1587–1606.

Kubar, T. L., D. E. Waliser, and J.-L. Li, 2011: Boundary layer and cloud structure controls on tropical low cloud cover using A-Train satellite data and ECMWF analyses. *J. Climate,* **24,** 194–215.

Li, J.-L. F., 1994: On shallow cumulus parameterization schemes for general circulation model planetary boundary layers. Ph.D. thesis, University of Wisconsin—Madison, 203 pp.

Ma, C.-C., C. R. Mechoso, A. W. Robertson, and A. Arakawa, 1996: Peruvian stratus clouds and the tropical Pacific circulation: A coupled ocean–atmosphere GCM study. *J. Climate,* **9,** 1635–1645.

Minnis, P., and E. F. Harrison, 1984: Diurnal variability of regional cloud and clear-sky radiative parameters derived from GOES data. Part II: November 1978 cloud distributions. *J. Climate Appl. Meteor.,* **23,** 1012–1031.

Mitchell, T. P., and J. M. Wallace, 1992: The annual cycle in equatorial convection and sea surface temperature. *J. Climate,* **5,** 1140–1156.

Norris, J. R., 1998a: Low cloud type over the ocean from surface observations. Part I: Relationship to surface meteorology and the vertical distribution of temperature and moisture. *J. Climate,* **11,** 369–382.

——, 1998b: Low cloud type over the ocean from surface observations. Part II: Geographical and seasonal variations. *J. Climate,* **11,** 383–403.

——, and C. B. Leovy, 1994: Interannual variability in stratiform cloudiness and sea surface temperature. *J. Climate,* **7,** 1915–1925.

——, and S. A. Klein, 2000: Low cloud type over the ocean from surface observations. Part III: Relationship to vertical motion and the regional surface synoptic environment. *J. Climate,* **13,** 245–256.

Oreopoulos, L., and R. Davies, 1993: Statistical dependence of albedo and cloud cover on sea surface temperature for two tropical marine stratocumulus regions. *J. Climate,* **6,** 2434–2447.

Philander, S. G. H., D. Gu, D. Halpern, G. Lambert, N.-C. Lau, T. Li, and R. C. Pacanowski, 1996: Why the ITCZ is mostly north of the equator. *J. Climate,* **9,** 2958–2972.

Platnick, S., M. D. King, S. A. Ackerman, W. P. Menzel, B. A. Baum, J. C. Riedi, and R. A. Frey, 2003: The MODIS cloud products: Algorithms and examples from Terra. *IEEE Trans. Geosci. Remote Sens.,* **41,** 459–473.

Randall, D. A., and M. J. Suarez, 1984: On the dynamics of stratocumulus formation and dissipation. *J. Atmos. Sci.,* **41,** 3052–3057.

Rodwell, M. J., and B. J. Hoskins, 2001: Subtropical anticyclones and summer monsoons. *J. Climate,* **14,** 3192–3211.

Ronca, R. E., and D. S. Battisti, 1997: Anomalous sea surface temperatures and local air–sea energy exchange on intraannual time scales in the northeastern subtropical Pacific. *J. Climate,* **10,** 102–117.

Rozendaal, M. A., C. B. Leovy, and S. A. Klein, 1995: An observational study of the diurnal cycle of marine stratiform cloud. *J. Climate,* **8,** 1795–1809.

Simmons, A., S. Uppala, D. Dee, and S. Kobayashi, 2006: ERA-Interim: New ECMWF reanalysis products from 1989 onwards. *ECMWF Newsletter,* No. 110, ECMWF, Reading, United Kingdom, 25–35. [Available online at http://www.ecmwf.int/publications/newsletters/pdf/110_rev.pdf.]

Stephens, G. L., 2005: Cloud feedbacks in the climate system: A critical review. *J. Climate,* **18,** 237–273.

Stine, A. R., P. Huybers, and I. Y. Fung, 2009: Changes in the phase of the annual cycle of surface temperature. *Nature,* **457,** 435–440.

Takahashi, K., 2005: The annual cycle of heat content in the Peru current region. *J. Climate,* **18,** 4937–4954.

——, and D. S. Battisti, 2007: Processes controlling the mean tropical Pacific precipitation pattern. Part I: The Andes and the eastern Pacific ITCZ. *J. Climate,* **20,** 3434–3451.

Warren, S. G., C. J. Hahn, J. London, R. M. Chervin, and R. L. Jenne, 1988: Global distribution of total cloud cover and cloud type amounts over the ocean. NCAR Tech. Note NCAR/TN−317+STR, 42 pp. + 170 maps.

Weng, F. Z., and N. C. Grody, 1994: Retrieval of cloud liquid water using the special sensor microwave imager (SSM/I). *J. Geophys. Res.,* **99,** 25 535–25 551.

Williams, K. D., and Coauthors, 2006: Evaluation of a component of the cloud response to climate change in an intercomparison of climate models. *Climate Dyn.,* **26,** 145–165.

Wood, R., 2012: Stratocumulus clouds. *Mon. Wea. Rev.,* **140,** 2373–2423.

——, and C. S. Bretherton, 2006: On the relationship between stratiform low cloud cover and lower-tropospheric stability. *J. Climate,* **19,** 6425–6432.

——, ——, and D. L. Hartmann, 2002: Diurnal cycle of liquid water path over the subtropical and tropical oceans. *Geophys. Res. Lett.,* **29,** 2092, doi:10.1029/2002GL015371.

Wylie, D., B. B. Hinton, and K. Kloesel, 1989: The relationship of marine stratus clouds to wind and temperature advection. *Mon. Wea. Rev.,* **117,** 2620–2625.

Xu, K.-M., T. Wong, B. A. Wielicki, L. Parker, and Z. A. Eitzen, 2005: Statistical analyses of satellite cloud object data from CERES. Part I: Methodology and preliminary results of the 1998 El Niño/2000 La Niña. *J. Climate,* **18,** 2497–2514.

Yu, J.-Y., and C. R. Mechoso, 1999: Links between annual variations of Peruvian stratocumulus clouds and of SST in the eastern equatorial Pacific. *J. Climate,* **12,** 3305–3318.

Zuidema, P., and D. L. Hartmann, 1995: Satellite determination of stratus cloud microphysical properties. *J. Climate,* **8,** 1638–1657.

——, D. Painemal, S. D. Szoeke, and C. Fairall, 2009: Stratocumulus cloud-top height estimates and their climatic implications. *J. Climate,* **22,** 4652–4666.